EFFECT OF SUPPORT MATERIAL IN NO$_X$ STORAGE/REDUCTION CATALYSTS

A THESIS SUBMITTED TO
THE GRADUATE SCHOOL OF NATURAL AND APPLIED SCIENCES
OF
MIDDLE EAST TECHNICAL UNIVERSITY

BY

RUSLAN HUMMATOV

IN PARTIAL FULFILLMENT OF THE REQUIREMENTS
FOR
THE DEGREE OF MASTER OF SCIENCE
IN
PHYSICS

AUGUST 2010

Approval of the thesis:

EFFECT OF SUPPORT MATERIAL IN NO$_X$ STORAGE/REDUCTION CATALYSTS

submitted by **RUSLAN HUMMATOV** in partial fulfillment of the requirements for the degree of **Master of Science in Physics Department, Middle East Technical University** by,

Prof. Dr. Canan Özgen
Dean, Graduate School of **Natural and Applied Sciences**

Prof. Dr. Sinan Bilikmen
Head of Department, **Physics**

Assist. Prof. Dr. Hande Toffoli
Supervisor, **Physics, METU**

Assist. Prof. Dr. Daniele Toffoli
Co-supervisor, **Chemistry, METU**

Examining Committee Members:

Prof. Dr. Şakir Erkoç
Physics, METU

Assist. Prof. Dr. Hande Toffoli
Physics, METU

Assoc. Prof. Dr. Bayram Tekin
Physics, METU

Assist. Prof. Dr. Emrah Özensoy
Chemistry, Bilkent

Assoc. Prof. Dr. Sadi Turgut
Physics, METU

Date: **August 31, 2010**

I hereby declare that all information in this document has been obtained and presented in accordance with academic rules and ethical conduct. I also declare that, as required by these rules and conduct, I have fully cited and referenced all material and results that are not original to this work.

Name, Last Name: RUSLAN HUMMATOV

Signature   :

ABSTRACT

EFFECT OF SUPPORT MATERIAL IN NO$_X$ STORAGE/REDUCTION CATALYSTS

Hummatov, Ruslan

M.Sc., Department of Physics

Supervisor : Assist. Prof. Dr. Hande Toffoli

Co-Supervisor : Assist. Prof. Dr. Daniele Toffoli

August 2010, 45 pages

Energy need in transportation and industry is mainly met by fossil fuels. This causes consumption of resources and some environmental problems. Diesel and gasoline engines are developed to consume fuel efficiently in vehicles. Since these engines work in a low fuel to air ratio, it becomes difficult to reduce nitrogen oxide emission. For this reason NO$_x$ storage/reduction (NSR) catalysts have been developed. While engines are operating under lean conditions alkaline or alkaline-earth component of NSR catalysts capture nitrogen oxides and during fuel rich period stored nitrates are reduced to nitrogen and oxygen gases. To develop this technology, different system parameters, for example system components and reaction environments have been widely investigated experimentally. To supplement the experimental findings, binding energies and structural properties of NO$_x$ on different catalyst components have been investigated theoretically.

It has been experimentally observed that adding TiO$_2$ to other conventional support materials increases resistance against sulfur poisoning, which is one of the main problems concerning NSR catalysts. For this reason, in this thesis (001) and (101) anatase surfaces have been investigated. Moreover, the effects of barium oxide units and layers on the electronic properties

of the (001) anatase surface have been studied. To observe the effects of TiO_2 as a support component, interactions of NO_2 and SO_2 on the unsupported and anatase supported (100) BaO surfaces have been compared. A clear increase in sulfur resistance has been observed in the presence of TiO_2 in the catalyst under certain conditions.

ÖZ

NO$_X$ DEPOLAMA/İNDİRGEME KATALİZÖRLERİNDE ALTTAS MALZEMENİN KATALİZE ETKİSİ

Hummatov, Ruslan

Yüksek Lisans, Fizik Bölümü

Tez Yöneticisi : Yrd. Doç. Dr. Hande Toffoli

Ortak Tez Yöneticisi : Yrd. Doç. Dr. Daniele Toffoli

Agustos 2010, 45 sayfa

Ulaşım ve sanayideki enerji ihtiyacı büyük oranda fosil kaynaklı yakıtlardan karşılanmaktadır. Bu, kaynakların tükenmesi ve çevresel sorunlara neden olmaktadır. Yakıtın taşıtlarda daha verimli kullanılması için dizel ve gazla çalışan motorlar üretilmiştir. Bu motorlar daha küçük yakıt/hava oranında çalıştığı için nitrojen oksit salınımının azaltılması zorlaşmıştır. Bu nedenle NO$_x$ depolama/indirgeme (NSR) katalizörleri geliştirilmiştir. Motorda oksijen oranı fazla olduğu zaman katalizörün alkali veya alkali-toprak bileşeni nitrojen oksitleri tutulmakta, daha sonra yakıt oranı faz-la olduğu zaman depolanan nitratlar N$_2$ ve O$_2$ gazları olarak indirgenmektedir. NSR katalizörünü geliştirmek için sistem parametreleri, katalizör bileşenleri, reaksiyon ortamları deneysel olarak genişçe incelenmiştir. Ayrıca, teorik olarak nitrojen oksitlerin değişik katalizör bileşenleri üzrindeki bağlanma enerjisi ve yapısal özellikleri hesaplanmaktadır.

Titanyum dioksitin diğer oksitlerle karıştırılarak NSR katalizörünün ana problemlerinden olan sulfür zehirlenmesine karşı direnci artırdığı deneysel olarak gözlemlenmiştir. Bu nedenle, bu tezde (001) ve (101) TiO$_2$ anatase yüzeyleri incelendi. Barium oksit monomer ve katman-

larinin (001) anatase yüzeyinin elektronik yapısına etkisi çalışıldı. Daha sonra TiO$_2$'in alttaş malzame olarak kullanılmasının etkilerini gözlemlemek için, NO$_2$ ve SO$_2$'in desteklenmemiş, ve anatasla desteklenmiş (100) BaO yüzeyiyle etkileşmesi karşilaştırıldı. Titanyum dioksidin sulfür zehirlenmesine karşi etkisi yalnız belirli durumlarda gözlemlendi.

Anahtar Kelimeler: Yoğunluk Fonksiyoneli Teorisi, NO$_x$ Depolama/İndirgeme, Katalizör, Titanyum Dioksit, Anatase

To my family.

ACKNOWLEDGMENTS

TABLE OF CONTENTS

LIST OF TABLES

LIST OF FIGURES

FIGURES

CHAPTER 1

INTRODUCTION

Energy supply has been one of the most challenging concerns of the world in recent times. Although considerable effort has been put forth for meeting the demand by the renewable and clean sources like sunlight, wind, geothermal sources etc., fossil fuels are still used widely in the industrial applications and transportation. The most concerning drawback of this application is environmental issues. The released exhaust contains gases like carbon monoxide (CO), hydrocarbons (HCs), nitrogen oxides (NO_x: NO and NO_2) and many others that can cause many environmental and health problems. Environmental catalysis is defined as the chemical processes that reduce the emission of the environmentally harmful compounds [1]. The main goal in this field is to convert harmful CO, HCs, NO_x gases to harmless and naturally abundant CO_2, N_2 and H_2O.

Nitrogen oxides can cause several environmental and health problems. Excessive amount of nitrogen oxides in the stratosphere destroys its ability of protection of the Earth from harmful ultraviolet lights coming from the Sun [2]. Moreover, in the clouds NO_x react with the hydroxyl (OH^-) to form nitric acid (HNO_3), that combines with the rain and lead to acid rains, causing serious ecosystem problems potentially leading to biological death of lakes and rivers [3].

It is reported that NO is an important messenger in the bloodstream that warns the white blood cells to destroy foreign bacteria and tumor cells [4]. On the other hand, when taken in excess amounts into the lungs it diffuses through capillary vessels and destroys the alveolar structure of lungs, causing some allergies like bronchitis, emphysema and asthma. Concentrations of

1

300 mg NO_2/m^3, usually found nearby many industrialized areas, can cause dangerous and permanent health problems [5].

The main source of the nitrogen oxides is fossil fuel combustion in the form of petroleum, gasoline, diesel and coke. Road transportation accounted for 40 % of the NO_x emission in 2005, followed by power plants (22 %), industry (16%), off-road transportation (15 %) and the residential sector (7 %) [6]. Several regulations have been set to have strict control on NO_x emission in transportation. These regulations vary depending upon countries and type of vehicles. European countries started to set such standards with Euro I in 1992. Limitations on the amount of the pollutant components increases each year while NO_x receding technology is developing [7] (Table 1.1).

Table 1.1: NO_x emission (g/km) standards in Europe for different vehicles and with implementation year. PC – personal cars, LDV – light dirty vehicles, HDV – heavy dirty vehicles

Standart	Year	Gasoline PCs and LDVs	Diesel PCs and LDVs	HDVs
Euro I	1992	0.62	0.90	8.0
Euro II	1996	0.35	0.67	7.0
Euro III	2000	0.15	0.50	5.0
Euro IV	2005	0.08	0.25	3.5
Euro V	2010 (2008)	0.06	0.18	2.0
Euro VI	2015 (2014)	0.06	0.08	0.4

There are two main generation processes of NO in the exhaust. The first one is the production by reaction of nitrogen and oxygen at high temperatures during burning of fuel in the engines, and the second one is the fact that nitrogen oxide can already exist in the content of the fuel naturally. Several technologies are used in industry and transportation to reduce nitrogen oxides; important ones will be introduced herein.

Firstly, selective catalytic reduction (SCR) technology was developed to reduce NO_x. Although it was formerly preferred for stationary sources like industrial boilers, recently it is applied in diesel engines of large ships, locomotives and automobiles. In this technology, reduction of NO_x is achieved by aqueous ammonia or urea in some ceramic carrier material like oxides of vanadia, zeolites and titania [8].

Secondly, three-way catalytic converters (TWC) were introduced to reduce pollutants from exhaust of vehicles. Its three main tasks are to reduce NO_x to nitrogen and oxygen, convert CO to harmless CO_2 and oxidize HC to carbon dioxide and water [9]. Although, this technology performs efficiently for the engines working slightly above the stoichiometric ratio, for lean-burn engines where fuel consumption is reduced by working at bigger air-fuel ratio, TWC is not efficient.

The main goal of automotive industry is to produce more efficient and lower-emission vehicles. Lean-burn gasoline and diesel engines have been developed in this perspective. Although these are more efficient than the conventional engines, removal of NO_x in an oxygen rich environment became a challenging problem for traditional three-way catalysts. To this purpose NO_x storage-reduction (NSR) catalysts are introduced.

1.1 NO_x Storage-Reduction Catalyst

Traditional engines work in stoichiometric (14.5:1) air-fuel ratio, which produces the right balance of CO, H_2 and HC to oxidize nitrogen oxides (NO_x). On the other hand, lean-burn engines increase efficiency by operating at a very high (25:1 and above) air-fuel ratio, but produce excess oxygen that makes difficult to remove NO_x for the conventional three-way catalyst. In 1994 Toyota developed a new catalyst technology that captures NO_x in excess oxygen, NO_x storage-reduction (NSR) catalyst. The main components of the NSR catalyst are a precious metal (Pt), an alkaline and alkaline earth metal oxide as a storage component (BaO), and a support material (γ-Al_2O_3). During the oxygen rich (lean-burn) period, NO_x is oxidized on Pt and stored on BaO in the form of $Ba(NO_3)_2$ [10]:

$$NO \xrightarrow[Pt]{O_2} NO_2 \xrightarrow[BaO]{O_2} Ba(NO_3)_2 \tag{1.1}$$
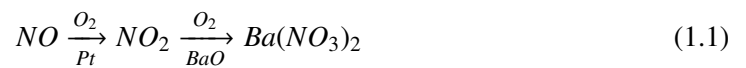
During the oxygen-deficient period $Ba(NO_3)_2$ is reduced to N_2 and BaO:

$$Ba(NO_3)_2 \xrightarrow{HC,H_2,CO} BaO + NO_2 \xrightarrow[Pt]{HC,H_2,CO} N_2 + CO_2 + H_2O \tag{1.2}$$
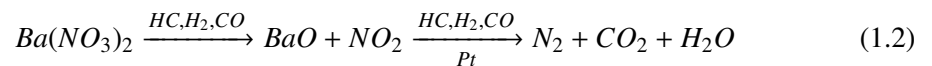
Since it is the most promising catalyst, the Pt-Ba/Al_2O_3 systems have been widely investigated. An uptake mechanism study of NO_x on Pt/BaO/Al_2O_3 catalyst [11] suggests that NO is firstly oxidized over Pt and then transferred to neighboring BaO. This mechanism is very

fast and converts NO_x completely but stops when a certain amount of $Ba(NO_3)_2$ is formed around Pt. Experiments using propylene as a reducing agent in the $Pt/BaO/Al_2O_3$ catalyst [12] indicate that storage of NO_x occurs first on BaO and then on $BaCO_3$ and $Ba(OH)_2$. The reduction of NO_x is fast at 250-400 °C and is limited by the C_3H_6 concentration. Moreover, there is small reduction of NO_x in form of NO and N_2O. In addition to these, different materials have been widely investigated as the NSR component to obtain cheaper, efficient catalysts with long-term durability to poisoning and high temperature.

1.2 Noble Metal Investigations

Since it is the initial promoter of NO_x oxidation, the performance of NSR catalysts strongly depends on the chemical and physical properties of the precious metal. Particle size effect investigation of Pt in $Pt/BaO/Al_2O_3$ [13] showed that for maintenance of NSR activity, retention of small Pt particles after thermal aging is very important. Using Pt as a noble metal in NSR has economical disadvantages in commercial applications. Investigations aim to replace it completely or decrease its amount by combination with some other noble metals.

Due to its similar chemical properties, palladium is a good candidate to be used instead of platinum. A comparative study [14] on NO_x storage and reduction behavior of $Pt/BaO/Al_2O_3$ and $Pd/BaO/Al_2O_3$ revealed that the catalyst with Pd showed higher NO_x reduction between 250 and 375 °C, which can promote NSR activation at low temperatures and under lean conditions. On the other hand, effect of cobalt and rhodium as a promoter on NO_x storage and reduction of $Pt/BaO/Al_2O_3$ catalyst were investigated [15]. It is reported that loading 2 % cobalt shows the highest NO_x uptake during the lean period but the poorest reduction in the rich period. On the other hand loading rhodium decreases NO_x uptake in lean period but increases reduction during the rich period.

From a computational point of view, adsorptions of NO_x on pseudomorphic mono-layer catalysts were investigated [16] with one layer of Pt or Pd supported by three layers of late transition metal supports (Cu, Ru, Rh, Ag, Ir and Au) and compared with four layers of Pt and Pd. It was observed that NO and oxygen atom adsorbs on Pt/Au and Pt/Ag more strongly

than the others, probably due to expansion of lattice on these hosts, whereas NO_2 adsorption was not affected from changes in lattice parameters.

1.3 Storage Component Investigations

After being oxidized over the noble metal in the lean period, NO_x are stored on the storage component of catalysts until the rich period. Stability of the adsorbates in this time interval is very important, as they could be released before being reduced to N_2 and O_2. Investigations of the storage component are done with the aim to find one with high storage capacity, with fast reducing ability and with strong interaction with the other components.

Sakamoto et al. [17] compared the NO_x regeneration process on $Pt/Ba/Al_2O_3$ and $Pt/K/Al_2O_3$. According to their observations NO_x is initially adsorbed as nitrite, then converted to nitrate forming $Ba(NO_3)_2$ and KNO_3, then these nitrates are reduced to N_2, NH_3 and H_2O by using H_2. They observed that there is a tendency for NH_3 release at high temperatures in the $Pt/Ba/Al_2O_3$ case, while at low temperatures in the $Pt/K/Al_2O_3$ case. The selectivity of NH_3 over N_2 depends on the ratio of stored NO_x and supplied H_2. The rate of NO_x release from potassium is faster than the one on barium.

Since there are small contradictions between stabilities of similar adsorption configurations of NO_2 over BaO, that were simulated by using different computational methods, Cheng and Ge [18] studied NO_2 adsorption on unsupported stoichiometric and non-stoichiometric BaO clusters, perfect and defective BaO surfaces, and γ-Al_2O_3 supported BaO clusters by using calculated binding energies and Bader charge analysis at the DFT level. The interactions of NO_2 with the stoichiometric cluster edge and corner sites are stronger than the interactions with the (100) BaO surface. Moreover, NO_2 interaction with the non-stoichiometric clusters is stronger than the interactions with the stoichiometric ones. In the case of γ-Al_2O_3 supported catalysts, preferable sites occur at the interface between BaO and γ-Al_2O_3. Moreover, the binding energies of NO_2 on supported $(BaO)_2$ clusters are significantly bigger than the unsupported ones, but for $(BaO)_4$ the trend is reversed. This means that the interaction is strongly morphology dependent.

1.4 Support Material Investigations

Although not a direct participant in the catalytic processes, the support material can significantly effect the performance of the catalytic components. Baiker et al. [19] investigated the effect of the support and Ba loading on NO_x storage-reduction in 1 wt % Pt loaded Pt-Ba/MO_2 (MO_2=SiO_2, CeO_2, ZrO_2) catalyst and compared them with the Pt/Al_2O_3 catalyst. In the Ba free case, the CeO_2 supported catalyst exhibits the highest NO_x storage, where ZrO_2 and SiO_2 supported ones showed lower and no storage, respectively. Ba loading increases NO_x storage for all catalysts and amount of loading effects the result significantly: up to 10 wt % CeO_2 showed the highest storage capacity, then for highest loading (28 wt %) ZrO_2 and Al_2O_3 showed similar and high capacity. The stability of stored NO_x is also loading dependent, and Al_2O_3 and CeO_2 showed similar fast reduction of NO_x while ZrO_2 showed slower.

On the other hand, since BaO and γ-Al_2O_3 are the most promising components for the NSR system, Mei et al. [20] investigated BaO adsorptions on (100) and (110) γ-Al_2O_3 surfaces. They have reported that the strongest bindings occurs when Ba interacts with numerous surface oxygens and O sits atop the fivefold aluminum atom. Moreover, there is significant relaxation on alumina surface, and aggregations of BaO occurs at high loadings. In addition to this, Szanyi et al. [21] simulated BaO monomer and dimer on (100) γ-Al_2O_3 surface and investigated NO_x adsorption on this catalyst and related this with experimental study. They reported that surface nitrates in infrared spectroscopy experiments are those nitrates interacting with BaO and $(BaO)_2$, and bulk nitrates are those interact with bulk BaO. Although it is initial oxidation component of catalysts Grönbeck et al. [22] used platinum as a support for BaO layers. The stability of NO_2 adsorption on Pt supported catalysts was bigger than adsorptions on unsupported BaO layers.

1.4.1 Sulfur poisoning and TiO$_2$ support

Sulfur oxides in the exhaust, present due to the sulfur compounds in the fuel, react with the catalyst components like nitrogen oxide, but sulfates are more stable than nitrates [10] and deactivate the catalyst. This is called "sulfur poisoning" and is the most difficult problem regarding the NSR. Sulfur poisoning occurs in both BaO through the formation of $BaSO_4$ and

in γ-Al_2O_3 with the formation of $Al_2(SO_4)$. TiO_2 combined with γ-Al_2O_3 and/or ZrO_2 are promising choices for sulfur tolerance [23].

An investigation of NO oxidation on Pt/TiO_2 has been carried out in the absence/presence of SO_2 [24]. Absence of SO_2 decreased nitrate intensities, that showed negative effect of SO_2 on nitrate formation, and small intensities of SO_2 indicates that TiO_2 has resistance to this species. It is reported that in addition to its ability to suppress sulfur adsorption, TiO_2 promotes sulfate decomposition through the interface between Al_2O_3 and TiO_2 due to its smaller particle size [10]. Despres et al. [25] reports that TiO_2 contributes to the NO_x storage capacity of BaO/TiO_2. In their work, Özensoy et al. [23] states that adding TiO_2 to Ba/γ-Al_2O_3 lowered the temperature for total decomposition of nitrates. Moreover, with the aim to obtain thermally stable and sulfur resistant catalyst, Takahashi et al. [26] investigated Pt/K catalyst supported with ZrO_2, TiO_2 and their mixture to see the effect of composition. They observed that the potassium changes into the sulfate in the titania free catalyst and NO_x removal becomes very poor. Whereas in the catalysts that were supported with the mixtures, the titania resists to potassium-sulfate formation, the zinconia suppressed solid-phase reaction with potassium. The composition with 70 wt%ZrO_2-30 wt%TiO_2 showed the highest NO_x removal ability.

Although TiO_2 is one of the promising candidates to increase sulfur tolerance, a DFT investigation of TiO_2 as a component of NSR catalyst is still missing. In this thesis we have investigated the effect BaO loadings on the electronic properties of (001) TiO_2 anatase surface, and the effect of anatase on the stability of NO_2 and SO_2 adsorptions on (100) BaO surface.

This thesis consists of four chapters. In the Chapter 2, density functional theory (DFT) is introduced. In the third chapter, results of DFT calculations are discussed, and a summary is provided in the conclusion section.

CHAPTER 2

DENSITY FUNCTIONAL THEORY

There is a great contribution of solid state physics in the development of various technologies in the past century. This is achieved by characterizing properties of matter. To do this, a wide range of experimental and theoretical methods have been used. Density functional theory (DFT) is one of the theoretical tools that use the basic principles of quantum mechanics to calculate electronic properties of matter.

2.1 Many-Body Hamiltonian

In quantum mechanics, to describe any many-body system one needs to solve the Schrödinger equation and obtain the many-body wave function:

$$\hat{H}\psi(\vec{r_1}, \ldots, \vec{r_N}; \vec{R_1}, \ldots, \vec{R_M}) = E\psi(\vec{r_1}, \ldots, \vec{r_N}; \vec{R_1}, \ldots, \vec{R_M}). \tag{2.1}$$

Here ψ is the many-body wave function which depends on the positions of electrons and nuclei, and $\hat{H}$ is the many-body Hamiltonian operator:

$$\hat{H} = \hat{T}_e + \hat{T}_n + \hat{V}_{ee} + \hat{V}_{en} + \hat{V}_{nn} \tag{2.2}$$

In Eq. (2.2) $\hat{T}_e$ is the kinetic energy of electrons, $\hat{T}_n$ is the kinetic energy of nuclei, $\hat{V}_{ee}$ is the Coulombic potential energy for electron-electron interaction, $\hat{V}_{en}$ is the Coulombic potential energy for electron-nuclei interaction and $\hat{V}_{nn}$ is the Coulombic potential energy for nuclei-nuclei interaction.

The total Hamiltonian for the nuclei at positions $\vec{R_I}$ with momenta $\vec{P_I}$ and for the electrons at

positions $\vec{r}_i$ with momenta $\vec{P}_i$ is:

$$\hat{H} = \sum_{I=1}^{N_I} \frac{\vec{P}_I^{\,2}}{2M} + \sum_{i=1}^{N_e} \frac{\vec{P}_i^{\,2}}{2m} + \frac{1}{2}\frac{1}{4\pi\epsilon_0} \sum_{I}^{N_I} \sum_{J\neq I}^{N_I} \frac{(Ze)^2}{|\vec{R}_I - \vec{R}_J|}$$
$$+ \frac{1}{2}\frac{e^2}{4\pi\epsilon_0} \sum_{i}^{N_e} \sum_{j\neq i}^{N_e} \frac{1}{|\vec{r}_i - \vec{r}_j|} - \frac{1}{4\pi\epsilon_0} \sum_{I=1}^{N_I} \sum_{i=1}^{N_e} \frac{Z_I e^2}{|\vec{r}_i - \vec{R}_I|} \qquad (2.3)$$

The nuclei are typically 2000–500000 times more massive than electrons, so they move typically 1000 times more slowly than electrons. In the Born-Oppenheimer approximation [27,28] the electrons are assumed to arrange themselves adiabatically around the nuclei, as the nuclei move. Since the positions of the nuclei are "fixed" the nuclei-nuclei potential energy term is constant, and it can be added at the end. The approximation is developed by separating the many-body wave function in the following way

$$\psi(\mathbf{r}, \mathbf{R}) = \sum_{n} \phi_m(\mathbf{R})\psi_{e,n}(\mathbf{r}, \mathbf{R}). \qquad (2.4)$$

In Eq. (2.4) $\mathbf{r}$, $\mathbf{R}$ denote the sets of the electron and nuclei position vectors, the set of $\psi_{e,n}(\mathbf{r}, \mathbf{R})$'s are the solutions of the electron-nuclei problem with the fixed nuclei, and $\phi_m(\mathbf{R})$ is the wave function of the nuclei. Moreover, it is clear that $\hat{T}_e$, $\hat{V}_{ee}$, $\hat{V}_{en}$ terms only operate on the electronic part of the product wave function, and give electronic energy $E_{e,n}$ for the fixed nuclei

$$(\hat{T}_e + \hat{V}_{ee} + \hat{V}_{en})\psi_{e,n}(\mathbf{r}, \mathbf{R}) = E_{e,n}(\mathbf{R})\psi_{e,n}(\mathbf{r}, \mathbf{R}). \qquad (2.5)$$

The electronic Hamiltonian is

$$\hat{H}_e = -\frac{\hbar^2}{2m_e} \sum_{i=1}^{N} \nabla_{\vec{r}_i}^2 + \frac{1}{2}\frac{e^2}{4\pi\epsilon_0} \sum_{i}^{N_e} \sum_{j\neq i}^{N_e} \frac{1}{|\vec{r}_i - \vec{r}_j|} - \frac{1}{4\pi\epsilon_0} \sum_{I=1}^{N_I} \sum_{i=1}^{N_e} \frac{Z_I e^2}{|\vec{r}_i - \vec{R}_I|}. \qquad (2.6)$$

A more convenient set of units are the atomic units where distances are written in terms of the Bohr radius a_0 – average radius of hydrogen atom in its ground state:

$$a_0 = \frac{4\pi\epsilon_0 \hbar^2}{m_e e^2}, \qquad (2.7)$$

and the energies are written in Hartree – twice the energy of the electron in the hydrogen atom in the ground state

$$E_h = \frac{\hbar^2}{2m_e a_0^2} = \frac{e^2}{8\pi\epsilon_0}. \qquad (2.8)$$

The electronic Hamiltonian can thus be written as:

$$\hat{H}_e = -\frac{1}{2} \sum_{i=1}^{N_e} \nabla_{\vec{r}_i}^2 + \frac{1}{2} \sum_{i}^{N_e} \sum_{j\neq i}^{N_e} \frac{1}{|\vec{r}_i - \vec{r}_j|} - \sum_{I=1}^{N_I} \sum_{i=1}^{N_e} \frac{Z_I}{|\vec{r}_i - \vec{R}_I|}. \qquad (2.9)$$

This many-body Hamiltonian results in a Schrödinger equation that needs to be solved for a wavefunction of 4N degrees of freedom. The exact solution of such a system is possible only in very small systems.

2.2 Density-based description of the many-body problem.

Instead of dealing with the wavefunction that has 4N (3 position, 1 spin for each electron) variables, DFT proposes a density, which is obtained from the true many-body wavefunction, with only one position variable. The idea of using the density as a fundamental variable comes from the early studies in quantum mechanics by L. H. Thomas [29] and E. Fermi [30], and it is used in calculating the electrostatic potential energy of the electron-electron interaction in Hartree theory [31]. But using the density as a unique variable including the kinetic energy term in the many-body problem was introduced by Hohenberg and Kohn [32].

2.2.1 Electron Density

The one-particle density operator for the N-electron system is defined as

$$\hat{n}(\vec{r}) = \sum_i^N \delta(\vec{r} - \vec{r}_i).$$

(2.10)

These delta functions count the contributions of each electron positioned at point $\vec{r}_i$ at point $\vec{r}$. Like other observables in quantum mechanics, the electron density is given as the expectation value of the corresponding operator:

$$n(\vec{r}) = \langle \psi | \hat{n}(\vec{r}) | \psi \rangle = \sum_{i=1}^N \int \delta(\vec{r} - \vec{r}_i) |\psi(\vec{r}_1, \ldots, \vec{r}_N)|^2 d\vec{r}_1 ... d\vec{r}_N$$

$$= \int \delta(\vec{r} - \vec{r}_1) |\psi(\vec{r}_1, \vec{r}_2, \ldots, \vec{r}_N)|^2 d\vec{r}_1 d\vec{r}_2 ... d\vec{r}_N$$

$$+ \int \delta(\vec{r} - \vec{r}_2) |\psi(\vec{r}_1, \vec{r}_2, \ldots, \vec{r}_N)|^2 d\vec{r}_1 d\vec{r}_2 ... d\vec{r}_N + ...$$

(2.11)

Using the properties of delta function:

$$n(\vec{r}) = \int |\psi(\vec{r}, \vec{r}_2, \ldots, \vec{r}_N)|^2 d\vec{r} d\vec{r}_2 ... d\vec{r}_N + \int |\psi(\vec{r}_1, \vec{r}, \ldots, \vec{r}_N)|^2 d\vec{r}_1 d\vec{r} ... d\vec{r}_N + ...$$

(2.12)

Reordering and relabeling the electronic variables yields

$$n(\vec{r}) = N \int |\psi(\vec{r}, \vec{r}_2 \ldots, \vec{r}_N)|^2 d\vec{r}_2 d\vec{r}_3 ... d\vec{r}_N$$

(2.13)

Integrating both sides of the Eq. (2.13) yields the expected normalization condition: the integral of the density over all space gives the total number of electrons, N:

$$\int d\vec{r}\, n(\vec{r}) = N \tag{2.14}$$

2.2.2 Energy in Terms of Density

DFT promotes the solution of the many-body Schrödinger equation by expressing every term in the energy expression as a functional of the density. The true kinetic energy of the system can be calculated by taking the expectation value of the kinetic energy operator:

$$\langle \psi(\vec{r_1}, \ldots, \vec{r_N}) | \hat{T}_e | \psi(\vec{r_1}, \ldots, \vec{r_N}) \rangle = -\frac{1}{2} \sum_{i=1}^{N} \int \psi(\vec{r_1}, \ldots, \vec{r_N}) \nabla^2_{\vec{r_i}} \psi(\vec{r_1}, \ldots, \vec{r_N}) \tag{2.15}$$

Eq. (2.15) can not be reduced to an expression in terms of the density since there is a second order derivative of the wavefunction in the kinetic energy operator. To deal with this problem Kohn and Sham [33] proposed a description in terms of an auxiliary system which possess an identical density to the true system but consists of non-interacting particles

$$n(\vec{r}) = \sum_{n}^{N_e} |\phi_n(\vec{r})|^2. \tag{2.16}$$

The kinetic energy of such a system is given by:

$$T = -\frac{1}{2} \sum_{n}^{N_e} \int d\vec{r}\, \phi_n^*(\vec{r}) \nabla^2 \phi_n(\vec{r}) + \Delta T. \tag{2.17}$$

Instead of non-interacting particles, the electron motion is correlated and a term ΔT is added to correct any error coming from this fact.

Secondly, the electron-nuclei potential energy is written in terms of the electron density as follows:

$$\langle \psi(\vec{r_1}, \ldots, \vec{r_N}) | \hat{V}_{ne} | \psi(\vec{r_1}, \ldots, \vec{r_N}) \rangle = -\sum_{I=1}^{N_I} \sum_{i=1}^{N_e} \int \frac{Z_I}{|\vec{r_i} - \vec{R_I}|} |\psi(\vec{r_1}, \ldots, \vec{r_N})|^2 d\vec{r_1}...d\vec{r_N} \tag{2.18}$$

Here, following the same procedure as was done for the kinetic energy, and using Eq. (2.13) one obtains:

$$E_{ne} = -\sum_{I=1}^{N_I} \int n(\vec{r}) \frac{Z_I}{|\vec{r_i} - \vec{R_I}|} d\vec{r} = \int n(\vec{r}) V_{ne}(\vec{r}) d\vec{r} \tag{2.19}$$

Lastly we have to write the electron-electron potential energy, E_{ee}, in terms of the electron density. The expectation value reads:

$$\langle \psi(\vec{r_1}, \ldots, \vec{r_N}) | \hat{V}_{ee} | \psi(\vec{r_1}, \ldots, \vec{r_N}) \rangle = \frac{1}{2} \sum_{i}^{N_e} \sum_{j \neq i}^{N_e} \int \frac{1}{|\vec{r_i} - \vec{r_j}|} |\psi(\vec{r_1}, \ldots, \vec{r_N})|^2 d\vec{r_1}...d\vec{r_N} \tag{2.20}$$

Both summations are over electrons, thus when expanded, E_{ee} becomes:

$$E_{ee} = \frac{1}{2}\Big[\iint \frac{1}{|\vec{r_1} - \vec{r_2}|}d\vec{r_1}d\vec{r_2} \int |\psi(\vec{r_1}, \ldots, \vec{r_N})|^2 d\vec{r_3}d\vec{r_4}...d\vec{r_N} +$$
$$\iint \frac{1}{|\vec{r_1} - \vec{r_3}|}d\vec{r_1}d\vec{r_3} \int |\psi(\vec{r_1}, \ldots, \vec{r_N})|^2 d\vec{r_2}d\vec{r_4}...d\vec{r_N} + \ldots \Big] \quad (2.21)$$

This expression cannot be further reduced to one in terms of the one-particle density. Instead the two-particle density matrix must be used, which contains contribution of two electrons, positioned at point $\vec{r_i}$ and $\vec{r_j}$, together at point $\vec{r}$:

$$\hat{n}(\vec{r}, \vec{r'}) = \sum_i^{N_e} \sum_j^{N_e} \delta(\vec{r} - \vec{r_i})\delta(\vec{r'} - \vec{r_j}) \quad (2.22)$$

Following the same procedure as was done for the one-particle density one obtains the two-particle density:

$$n(\vec{r}, \vec{r'}) = \frac{N_e(N_e - 1)}{2} \int |\psi(\vec{r}, \vec{r'}, \vec{r_3} \ldots, \vec{r_N})|^2 d\vec{r_3}d\vec{r_4}...d\vec{r_N} \quad (2.23)$$

Here N_e electrons interact with each other without interacting with themselves so there are $\frac{N_e(N_e-1)}{2}$ terms representing all the pairs of electrons. Thus:

$$E_{ee} = \frac{1}{2}\frac{2}{N_e(N_e - 1)}\Big[\iint \frac{n(\vec{r_1}, \vec{r_2})}{|\vec{r_1} - \vec{r_2}|}d\vec{r_1}d\vec{r_2} + \iint \frac{n(\vec{r_1}, \vec{r_3})}{|\vec{r_1} - \vec{r_3}|}d\vec{r_1}d\vec{r_3} + \ldots \Big]$$
$$= \frac{1}{2}\iint \frac{n(\vec{r}, \vec{r'})}{|\vec{r} - \vec{r'}|}d\vec{r}d\vec{r'} \quad (2.24)$$

Assuming that a large part of the two-particle density is due to the uncorrelated part, one defines:

$$n(\vec{r}, \vec{r'}) = n(\vec{r})n(\vec{r'}) + \Delta n(\vec{r}, \vec{r'}) \quad (2.25)$$

Here the uncorrelated part gives rise to the potential energy that was already known as the Hartree energy; to correct for any contribution from the correlation, a term ΔE_{ee} is added:

$$E_{ee} = \frac{1}{2}\iint \frac{n(\vec{r})n(\vec{r'})}{|\vec{r} - \vec{r'}|}d\vec{r}d\vec{r'} + \Delta E_{ee} \quad (2.26)$$

Putting Eq. (2.17), Eq. (2.19), Eq. (2.26) together:

$$E = -\frac{1}{2}\sum_n^{N_e} \int d\vec{r}\phi_n^*(\vec{r})\nabla^2\phi_n(\vec{r}) + \int n(\vec{r})V_{ne}(\vec{r})d\vec{r}$$
$$+ \frac{1}{2}\iint \frac{n(\vec{r})n(\vec{r'})}{|\vec{r} - \vec{r'}|}d\vec{r}d\vec{r'} + \Delta E_{ee} + \Delta T \quad (2.27)$$

The correction in kinetic energy term, ΔT, together with the correction in the electron-electron potential term, ΔE_{ee}, defines the exchange correlation energy:

$$E_{xc} = \Delta T + \Delta E_{ee} \quad (2.28)$$

2.2.3 Exchange and Correlation Functionals

Electrons repel each other via the Coulomb force. That means that their motion is correlated, giving rise to the correction ΔT in Eq. (2.27). Furthermore, due to the fermionic property of the electrons, the many-body wavefunction must be antisymmetric with respect to the exchange of two electrons. These two effects together leads to the exchange-correlation energy, which is the only unknown part of the Kohn-Sham equations. Several approximations have been proposed to calculate the exchange-correlation energy. One of the well known approximations is the local density approximation (LDA), which is used for slightly varying densities $n(\vec{r})$, and defined as:

$$E_{xc}^{LDA} = \int n(\vec{r})\epsilon_{xc}[n(\vec{r})]d\vec{r} \tag{2.29}$$

Here $\epsilon_{xc}[n(\vec{r})]$ is the exchange-correlation energy per electron for a uniform electron gas with the density $n(\vec{r})$. Thus, this expression is exact for electrons in an infinite space which is made neutral by a uniform positive background. Values of $\epsilon_{xc}[n(\vec{r})]$ are obtained by Monte Carlo calculations [34] in practice.

To improve the accuracy beyond LDA for inhomogeneous systems, the generalized gradient approximation (GGA) was proposed. It takes into account further gradients of the density:

$$E_{xc}^{GGA} = \int f[n(\vec{r}), \nabla n(\vec{r})]d\vec{r} \tag{2.30}$$

2.3 Hohenberg-Kohn Theorems

The many-body Schrödinger equation has already been written in terms of the density (Eq. (2.27)). The kinetic energy term (Eq. (2.17)) consists of derivatives of single-particle orbitals which are related to the density (Eq. (2.16)); the Hartree term depends directly on the density (Eq. (2.26)), and the exchange-correlation part is approximated as a local functional of the density (Eq. (2.29, 2.30)) but the external potential is still not related with the density. In 1964 Hohenberg and Kohn proposed two theorems [32] that define DFT as a computational methodology. The first theorem states that there is a one-to-one correspondence between density and external potential, in other words the external potential is a unique functional of the density

$$v_{ext}(\vec{r}) \Leftrightarrow n(\vec{r}). \tag{2.31}$$

13

Hohenberg and Kohn didn't give any expression that relates the external potential and the density, but they proved this theorem by reductio ad absurdum (reduction by self-contradiction). In the proof firstly two different external potentials are assumed to give the same ground state density. Then it is shown that it is not possible, since the calculated total energies after interchanging the external potential for these two systems gives contradiction.

The second theorem states that the energy can be written in terms of the density, and the density that minimizes the energy is the ground state density.

$$E_0[n_{gs}] < E_0[n]. \tag{2.32}$$

Here E_0 is the ground state energy and n_{gs} is the ground state density. In fact, according to the variational principle, any density other than the ground state density will necessarily give a higher energy than the ground state energy. If the ground state electron density of the system is known, then the ground state wavefunction is known and then any ground state property can be found. Thus any observable is an unique functional of the density:

$$\langle \psi_0 | \hat{A} | \psi_0 \rangle = A[n] \tag{2.33}$$

2.4 Kohn-Sham Equations

According to the second theorem, the global minimum of the energy functional is reached at the ground state density. At the minimum, small changes in the energy functional due to small changes in density should be zero:

$$\delta E_e[n] \equiv E_e[n + \delta n] - E_e[n] = 0 \tag{2.34}$$

Minimization of the energy is done by using the undetermined Lagrange multipliers method with the constraint that the one-particle orbitals are orthonormal:

$$\delta\{E_e[n(\vec{r})] - \sum_{i,j} \lambda_{i,j}(\langle \phi_i | \phi_j \rangle - \delta_{ij})\} = 0 \tag{2.35}$$

Variation with respect to ϕ^* is equivalent to variation with respect to n, which yields

$$\frac{\delta}{\delta \phi_i^*(\vec{r})}\{E_e[n(\vec{r})] - \sum_{i,j} \lambda_{i,j}(\langle \phi_i | \phi_j \rangle - \delta_{ij})\} = 0 \tag{2.36}$$

14

In extended form:

$$\frac{\delta}{\delta\phi_i^*(\vec{r})}\left[-\frac{1}{2}\sum_n^{N_e}\int d\vec{r}\phi_n^*(\vec{r})\nabla^2\phi_n(\vec{r})\right]+$$

$$\frac{\delta}{\delta n(\vec{r})}\left[\int n(\vec{r})V_{ne}(\vec{r})d\vec{r} + \frac{1}{2}\iint \frac{n(\vec{r})n(\vec{r'})}{|\vec{r}-\vec{r'}|}d\vec{r}d\vec{r'}\right.$$

$$\left. + \int d\vec{r}n(\vec{r})\epsilon_{xc}(n(\vec{r}))\right]\frac{\delta n(\vec{r})}{\delta\phi_i^*(\vec{r})} = \epsilon_i\phi_i(\vec{r}) \quad (2.37)$$

Assuming the exchange-correlation functional ϵ_{xc} is also a simple function of density:

$$-\frac{1}{2}\nabla^2\phi_i(\vec{r}) + \left[V_{ne}(\vec{r}) + \int\frac{n(\vec{r})}{|\vec{r}-\vec{r'}|}d\vec{r'} + \epsilon_{xc}[n(\vec{r})] + n(\vec{r})\frac{\delta\epsilon_{xc}[n(\vec{r})]}{\delta n(\vec{r})}\right]\phi_i(\vec{r}) = \epsilon_i\phi_i(\vec{r}) \quad (2.38)$$

Here the collection of terms inside the square brackets defines the Kohn-Sham potential, V_KS, and a Schrödinger-like equation is obtained

$$[\hat{T} + V_{KS}]\phi_i(\vec{r}) = \epsilon_i\phi_i(\vec{r}). \quad (2.39)$$

It is very difficult, generally impossible to solve this equation analytically. In the following sections we give an overview of the several methods employed to acomplish this task.

2.5 Pseudopotentials

Electrons around the nuclei can be divided in two groups: core and valence electrons. The core electrons are strongly bound to the nuclei and are not affected from chemical interactions, but the valence electrons participate in the chemical bond and determine the electronic properties of matter. These electrons move in the field of the nuclei and the core electrons, which diverges around the nuclei and makes the valence orbitals to oscillate around this region. Since it requires much computational cost to expand the oscillatory wavefunction in terms of plane waves, to make valance states smoother in this region one describes the effects of the core electrons with an effective potential: a pseudopotential.

Pseudopotential generation starts with solving the all-electron Kohn-Sham equation for an isolated atom. Pseudowavefunctions are obtained by replacing the oscillatory part of the wavefunction inside a core region ($r < r_c$) with a smoother function. This wavefunction must match the true wavefunction outside the core region, and their norm squares must integrate to the same value inside r_c (a "norm-conserving" pseudopotential [35]). Then the Schrödinger
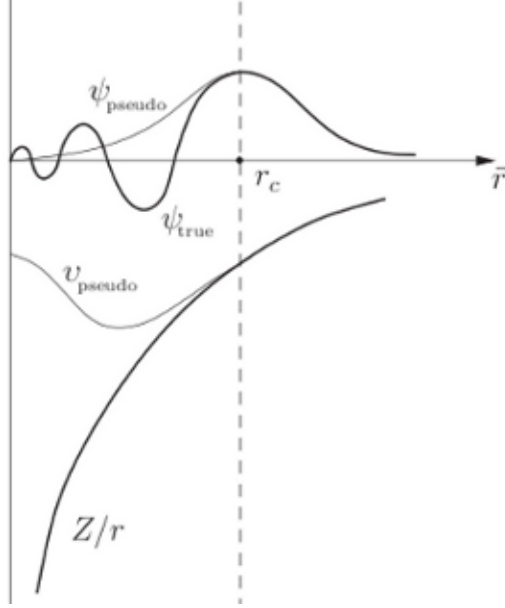
Figure 2.1: Real and pseudo wave function.

equation is inverted to obtain the pseudopotential, which must be identical to the true potential outside the core region. Moreover, the norm-conserving constraint is relaxed in pseudopotential generation to obtain smoother pseudowavefunctions that require a much smaller plane-wave cutoff [36]. Since it requires a much smaller number of plane-waves it is called "ultrasoft" pseudopotential. Each orbital has a different pseudopotential and the quality of the pseudopotential is determined by its transferability (ability to describe valance electrons in different type of systems), and by its efficiency (the requirement of a small plane-wave expansion).

2.6 Plane-wave Expansion

The Kohn-Sham approach together with the pseudopotential idea present several advantages to the solution of the many-body Schrödinger equation. The problem was converted to non-interacting single particle system, but still needs to be solved for an infinite number of electrons interacting with an infinite number of nuclei. For further simplification we restrict our attention to periodic systems where the effective potential has the periodicity of the lattice.

In the previous section, the Kohn-Sham equations have been defined (Eq. (2.39)), which can

be written in short form as

$$\hat{H}_{KS}\phi(\vec{r}) = \epsilon_i\phi_i(\vec{r}).\tag{2.40}$$

This equation is further converted into a matrix eigenvalue equation. This is achieved by expanding all terms in a suitable basis, here in a plane-wave basis. The Kohn-Sham orbitals can be written in terms of plane-waves as

$$\phi_i(\vec{r}) = \sum_{\vec{q}} c_{i,\vec{q}} \frac{1}{\sqrt{\Omega}} \exp(i\vec{q}.\vec{r}) \equiv \sum_{\vec{q}} c_{i,\vec{q}}|\vec{q}\rangle\tag{2.41}$$

where $c_{i,\vec{q}}$ are expansion coefficients and $\frac{1}{\sqrt{\Omega}}$ is introduced to satisfy the normalization:

$$\langle\vec{q}'|\vec{q}\rangle = \frac{1}{\Omega} \int_{\Omega} d\vec{r} \exp(-i\vec{q}'.\vec{r}) \exp(i\vec{q}.\vec{r}) = \delta_{\vec{q},\vec{q}'}.\tag{2.42}$$

To obtain the matrix form of Eq. (2.40), we insert Eq. (2.41), and multiply from left by the conjugate $\langle\vec{q}'|$ and integrate over the real space

$$\sum_{\vec{q}} \langle\vec{q}'|\hat{H}_{KS}|\vec{q}\rangle c_{i,\vec{q}} = \epsilon_i \sum_{\vec{q}} \langle\vec{q}'|\vec{q}\rangle c_{i,\vec{q}} = \epsilon_i c_{i,\vec{q}}\tag{2.43}$$

In matrix notation:

$$\bar{H}C = \epsilon_i C\tag{2.44}$$

where $\bar{H}$ is the Hamiltonian matrix and C is the vector of coefficients. In matrix representation, the kinetic energy term is in diagonal form:

$$\langle\vec{q}'| -\frac{1}{2}\nabla^2|\vec{q}\rangle = \frac{1}{2}|\vec{q}|^2\delta_{\vec{q},\vec{q}'}.\tag{2.45}$$

Since it has similar exponential terms, Fourier transform is used to express the effective potential in matrix form. The effective potential has the periodicity of the lattice, thus only terms with wavevectors $(\vec{G})$ of the reciprocal space of the periodic system contribute:

$$\hat{V}_{eff}(\vec{r}) = \sum_{m} \hat{V}_{eff}(\vec{G}_m) \exp(i\vec{G}_m\vec{r})\tag{2.46}$$

where

$$\hat{V}_{eff}(\vec{G}) = \frac{1}{\Omega_{cell}} \int_{\Omega_{cell}} \hat{V}_{eff}(\vec{r}) \exp(i\vec{G}_m\vec{r})d\vec{r}\tag{2.47}$$

Moreover, the expectation value of the effective potential term is given by:

$$\langle\vec{q}'|\hat{V}_{eff}|\vec{q}\rangle = \sum_{m} \langle\vec{q}'|\hat{V}_{eff}(\vec{G}_m)|\vec{q}\rangle \exp(i\vec{G}_m\vec{r})$$

$$\equiv \sum_{m} \langle\vec{q}'|\hat{V}_{eff}(\vec{G}_m)|\vec{q}+\vec{G}_m\rangle = \sum_{m} V_{eff}(\vec{G}_m)\langle\vec{q}'|\vec{q}+\vec{G}_m\rangle = \sum_{m} V_{eff}(\vec{G}_m)\delta_{\vec{q}'-\vec{q},\vec{G}_m}\tag{2.48}$$

Only basis elements with wavevectors that differs by a reciprocal wavevector ($\vec{q}' - \vec{q} = \vec{G}_m$) contributes to the effective potential term. To represent it completely in terms of $\vec{G}_m$ say $\vec{q} = \vec{k} + \vec{G}_m$ and $\vec{q}' = \vec{k} + \vec{G}_{m'}$, thus

$$\sum_m \left[\frac{1}{2} |\vec{k} + \vec{G}_m|^2 \delta_{m'm} + V_{eff}(\vec{G}_m - \vec{G}_{m'}) \right] c_{i,\vec{k}+\vec{G}} = \epsilon_i c_{i,m'}. \tag{2.49}$$

This is a matrix equation where the kinetic energy term is in a diagonal form and V_{eff} includes plane-wave representation of the external potential term, the Hartree potential term and the exchange correlation potential term. Considering accuracy and the computational cost in practice the plane-wave expansion is done up to some cutoff value ($\frac{1}{2}|\vec{G}|^2 < E_{cut}$).

2.7 Application of DFT

The calculations reported in this thesis were done by using the Quantum-Espresso (QE) package [37], which uses a Plane–Wave–Self–Consistent field (PWscf) approach within density functional theory. QE enables to calculate several electronic properties of solids and molecules. Solving the Kohn-sham equations self-consistently is the fundamental step of any DFT calculation. Any SCF calculation starts with a choice for the initial density depending on atom types and atomic positions. Then the Kohn-Sham equations are solved for Kohn-Sham orbitals. The new density obtained from these orbitals is compared with the old density. If the obtained density is consistent with the density, obtained from the previous cycle the calculation finishes, or else a second step starts from this density and the SCF loop continues until consistency is achieved.

2.7.1 Structure Relaxation

Investigation of any system with DFT starts with a structure relaxation. A relaxation calculation consists of several SCF calculations which is done to minimize energy. After each SCF calculation the forces on each atom are calculated by taking the derivative of the energy with respect to the position of the nuclei

$$F_i = -\frac{\partial E}{\partial R_i}. \tag{2.50}$$

In practice this is done by using the Hellmann-Feynman theorem [38,39]. The theorem states that the derivative of the energy with respect to any parameter can be obtained by calculating the expectation value of the derivative of the Hamiltonian operator with respect to the same parameter. In our case our parameters are the atomic positions, thus

$$
\begin{aligned}
F_i = -\frac{\partial}{\partial R_i}\langle\psi|\hat{H}|\psi\rangle &= -\langle\frac{\partial\psi}{\partial R_i}|\hat{H}|\psi\rangle - \langle\psi|\frac{\partial\hat{H}}{\partial R_i}|\psi\rangle - \langle\psi|\hat{H}|\frac{\partial\psi}{\partial R_i}\rangle \\
&= -E_{R_i}\langle\frac{\partial\psi}{\partial R_i}|\psi\rangle - E_{R_i}\langle\psi|\frac{\partial\psi}{\partial R_i}\rangle - \langle\psi|\frac{\partial\hat{H}}{\partial R_i}|\psi\rangle \\
&= -E_{R_i}\frac{\partial}{\partial R_i}\langle\psi|\psi\rangle - \langle\psi|\frac{\partial\hat{H}}{\partial R_i}|\psi\rangle = -\langle\psi|\frac{\partial\hat{H}}{\partial R_i}|\psi\rangle \quad (2.51)
\end{aligned}
$$

This is a very important result which means that the change in energy only depends on changes in the Hamiltonian but not on the change in the wavefunction. After calculating the forces on the atoms, each atom is moved to reduce the force and decrease the energy. These steps continues until a threshold force on each atom is achieved for a fixed cell-parameter.

It is possible to perform a variable-cell relaxation that changes the cell-parameters also to reduce stress on the cell. When the calculation is finished, the relaxed atomic positions and the total energy of cell are written in output file, and other important informations like real-space wavefunction, effective potential, electron density are put in a temporary directory for further analysis.

2.7.2   Band Structure Calculations

Electrons occupy discrete energy levels around a single atom, but when some number of atoms came together to form crystals those close energy levels form some continuous levels which are called bands. The band structure of the solid gives important information about electronic properties such that the energy gap between valance and conduction band which determines the type of solid. True band structure calculation involves the calculation of the energy for each k-point in the three dimensional Brillouin zone [40]. In practice bands are calculated on some path between certain critical points in Brillouin zone. One usually starts from the gamma point (center of the Brillouin zone) and joins points in the borders. In this study such paths are selected with the aid of XCrysDen [41]-visualization program also used to visualize structures in input and output files. For bulk and (001) surfaces with tetragonal

cells, the Brillouin zones are tetragonal with inverted cell parameters, and the chosen path is shown in Figure 2.2.
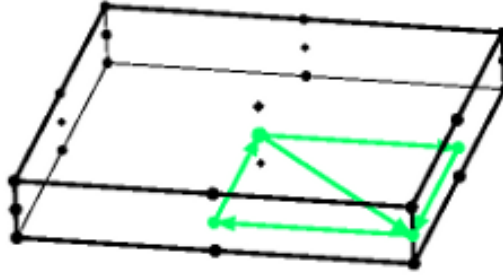

Figure 2.2: K-path for the band structure calculation of systems with tetragonal cell.

2.7.3   DOS & PDOS Calculation

Another important information about the solids is the density of states (DOS) that is number of states in a given energy interval. In the software suite used in this thesis, the DOS calculation is realized through a post-processing tool which increases the resolution of the discrete energy states by running a single-step of the self-consistent field calculation through a larger k-space sampling. A partial density of states (PDOS) calculation is used to perform a non-unique projection of the Kohn-Sham orbitals on to suitably defined atomic regions. This breakdown provides a qualitative analysis of charge transfer during chemical processes. The particular projection method used in this thesis is Löwdin population analysis [42].

CHAPTER 3

RESULTS and DISCUSSION

In this chapter, the (001) and (101) surfaces of TiO_2 anatase are investigated as a support for different BaO loadings for NO_x storage systems, and results are compared with those corresonding to the unsupported (100) BaO surface. Calculations reported in this study are done by using the Quantum-Espresso package, which solves Kohn-Sham equations by using a plane-wave expansion. The Pedrew–Burke–Ernzerhof [43] approximation is used for the exchange-correlation functional. The effects of the core electrons are described by ultrasoft [36] pseudopotentials, and the valence orbitals for electrons are expanded in the planewave basis set.

3.1 Titanium Dioxide

Titanium dioxide (TiO_2) has been studied extensively over the last few decades due to its wide range of industrial applications. Its areas of application include dielectrics in electronic devices [44], optical coatings [45], white pigment in paints [46], photocatalytic devices [47] and heterogeneous catalysts [48]. It has three polymorphs in nature: rutile, anatase and brookite (Figure 3.1). Due to its low stability brookite has received little interest for practical purposes. Rutile is the most stable, and other polymorphs are converted to rutile at high temperatures. Since it is relatively easy to obtain single crystals of rutile, its surface properties have been investigated experimentally. On the other hand, since it is difficult to obtain a sufficient amount of single anatase crystals, anatase surfaces are experimentally less explored. For several applications like photo-catalysis, dye-sensitized solar-cells, and catalysis anatase is more efficient than rutile due to its surface properties.
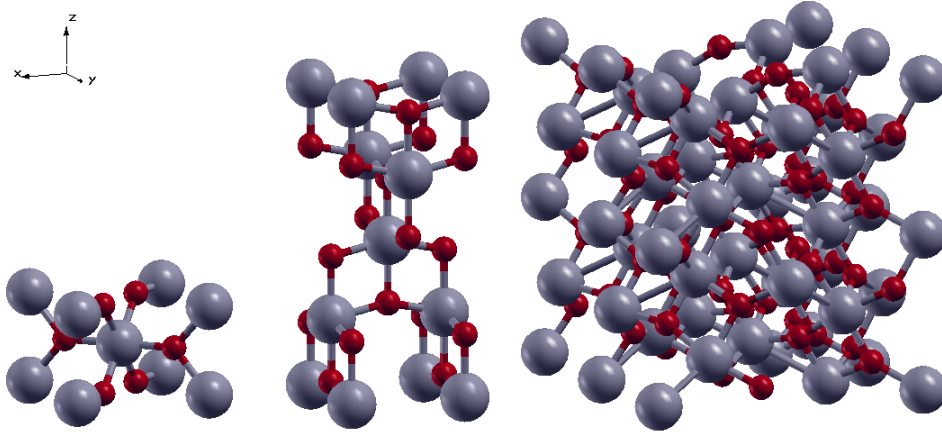
Figure 3.1: Three polymorphs of titania: rutile, anatase and brookite. Grey balls represent titanium atoms and red ones oxygen atoms.

3.2 Bulk Calculations of Anatase

Anatase has a tetragonal cell ($a = b \neq c$, $\alpha=\beta=\theta=90°$, Figure 3.1) with 4 TiO_2 units in the unit cell. The name "anatase" is Greek and means "exposed" due to its elongated shape in the vertical direction [48]. Each titanium atom coordinates six oxygen atoms forming octahedral TiO_6, and each oxygen is bound to two titanium atoms. There are two different bonds between titanium and oxygen atoms, vertical ones are referred to as apical bonds (1.979 Å) and the horizontal ones as equatorial bonds (1.932 Å).

Lattice-parameters of anatase are calculated through several optimization steps. Firstly, cell-parameters are optimized together to give the minimum energy with the fixed cell relaxation. As a result of a convergence study of cutoff energies, 40 Ry proved to be sufficient to yield a 10^{-4} Ry accuracy in the total energy. Then a variable-cell relaxation is performed with 10x10x5 k-points mesh, a 40 Ry kinetic energy cutoff and a 400 Ry cutoff for augmented electron density. Obtained cell-parameters (a=3.786 Å, c= 9.619 Å) are in good agreement with experimentally (3.782 Å, 9.502 Å [49]) and theoretically (3.786 Å, 9.737 Å [50]) obtained values from the literature.

As a further check, a band structure calculation is performed along high-symmetry directions for anatase bulk. The obtained band gap (2.1 ev) is significantly small than the experimental
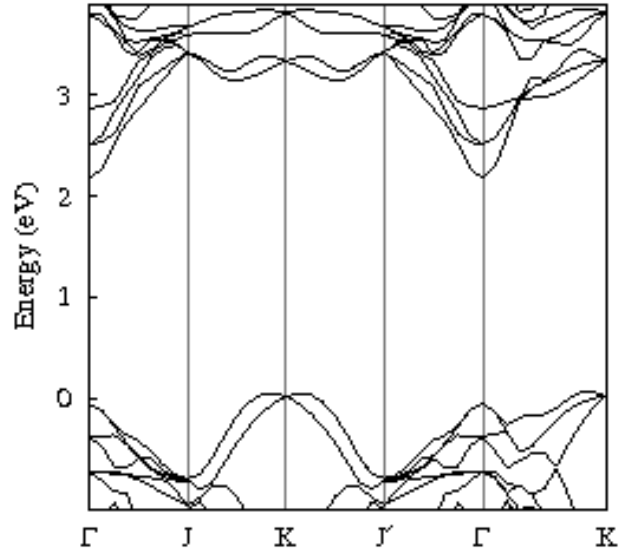
Figure 3.2: Band structure of anatase bulk along high symmetry directions.

value (3.2 eV [52]) but is very close to previous theoretical estimates and the general shape of the bands agrees with previous computational work [53].

3.3 Surface Calculations

In real-life applications matter interacts with the surroundings via its surfaces. Surface science studies are of great importance in many fields including membranes for gas separations, interfaces, semiconductor fabrication. Moreover, surface properties are crucial in chemical processes, especially in catalysis. Large surface area increases available adsorption sites for catalytic application and promotes storage capacity, and chemical activity of the surface directly effects device performance.

Stability of any surface is directly related to its surface energy. In planewave-based DFT software, surfaces are generated by periodically repeated slabs with atomic positions that are obtained from the bulk, with the addition of some vacuum after each slab. The surface energy of such surfaces are calculated from the difference in the energy of the same number of TiO_2

23

units in the slab and in the bulk divided by twice the surface area [50]:

$$E_{surf} = \frac{E_{slab} - (\frac{N_{slab}}{N_{bulk}})E_{bulk}}{2Area} \qquad (3.1)$$

Slabs with a suitable number of fixed bottom layers is a realistic way of describing surfaces. Reconstruction occurs also on slabs without fixed layers. Thus for asymmetric slabs, surface energies are calculated by subtracting the surface energy of the unrelaxed slab from the formation energy of the partially fixed slab [54]:

$$E_{surf-fixed} = \frac{E_{slab} - (\frac{N_{slab}}{N_{bulk}})E_{bulk}}{Area} - E_{surf(unrelax)} \qquad (3.2)$$

In this study calculations are performed with a vacuum of approximately 12-13 Å between slabs, and any dipole interaction between slabs is checked by using some larger values for the vacuum. Since the lattice vector along the c-axis of the unit cell is long, the Brillouin zone will be proportionally reduced to a very small value causing a dense folding of the bands. Thus a single k-point in this direction is sufficient for an accurate sampling.

3.3.1 Anatase (001) Surface

(001) is chemically the most active anatase surface. In this study it is obtained from the bulk by truncation. There are twofold and threefold coordinated oxygen atoms (O1, O2) and fivefold-coordinated titanium atoms (Ti1), that yield two oxygen and one titanium atoms per cell on the surface (Figure 3.3). Minimum-energy configurations are obtained by only a small initial distortion of the surface oxygen atom (O1). After relaxation the symmetry of (Ti1–O1–Ti1) bonds on the surface is broken by the shift of O1 towards one of the Ti1's. Displacements of surface atoms after reconstruction are in good agreement with previously reported study [50] (Table 3.1).

To find the optimal k-point mesh and the proper number of layers in the slab to describe the (001) anatase surface, surface energies are calculated with 4x4x1, 5x5x1 and 6x6x1 k-point meshes and for four, five and six layered slabs. There are negligible differences between the surface energies of the "all-free" slabs and partially fixed ones (Table 3.2). Slabs with six layers (two fixed) are chosen to describe the (001) anatase surface.
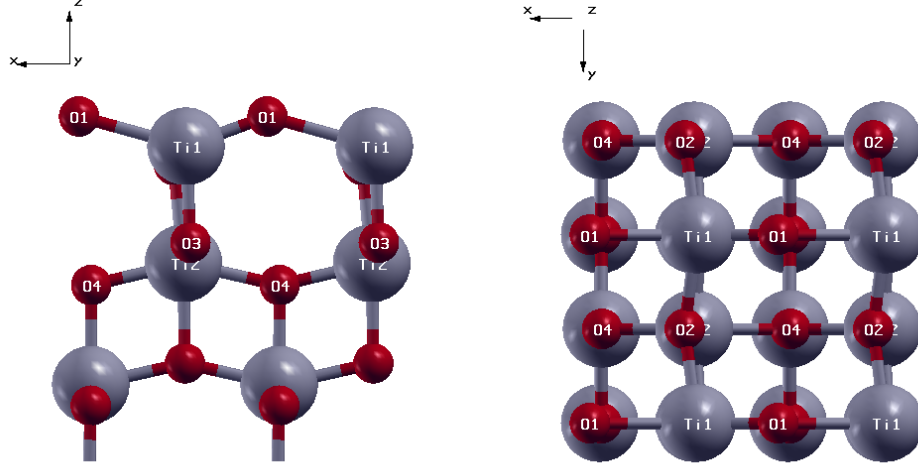
Figure 3.3: Side and top view of surface atoms of (001) anatase surface.

Table 3.1: Displacements of surface atoms for (001) anatase surface after reconstruction. Apical bonds (a) are 1.995 Å, and equatorial (e) ones are 1.938 Å. Values in parenthesis are from literature [50].

ID	Atomic Displacements (Å)			Bond Expansion	
	[100] (-x)	[010] (y)	[001] (z)	Label (type)	%
O1	-0.199 (-0.19)	0.00	0.201 (0.08)	Ti1-O1 (e)	+15.2 (+13.4)
O2	-0.184 (-0.17)	0.00	0.043 (-0.02)	Ti1-O2 (e)	+0.5 (+0.1)
O3	0.146 (0.11)	0.00	0.073 (0.01)	Ti1-O3 (e)	-2.9 (-3.4)
O4	0.046 (0.02)	0.00	0.037 (-0.00)	Ti2-O2 (a)	-0.7 (-1.2)
Ti1	0.057 (0.04)	0.00	0.014 (-0.06)	Ti2-O3 (e)	-1.7 (+0.1)
Ti2	0.005 (-0.01)	0.00	0.064 (0.01)	Ti2-O4 (e)	+3.7 (+1.9)
Ti3	0.035 (0.02)	0.00	0.031 (0.00)	Ti3-O4 (a)	+0.3 (-0.1)

Table 3.2: Surface energies of (001) anatase surfaces for four, five and six-layer slabs in J/m^2.

Layer/fixed (Eq.)	Ref. [50,51]	3x3x1	4x4x1	6x6x1
4/0 (3.1)	0.98	0.866	0.890	0.889
4/2 (3.2)		0.867	0.891	0.889
4/4 (3.1)		1.028	1.068	1.063
5/0 (3.1)		0.862	0.891	0.888
5/2 (3.2)		0.977	1.012	1.003
5/5 (3.1)		1.025	1.071	1.065
6/0 (3.1)	0.90	0.852	0.891	0.885
6/2 (3.2)		0.846	0.887	0.881
6/3 (3.2)		0.849	0.889	0.883
6/6 (3.1)		1.017	1.072	1.063

For k-point optimization several further calculations with a larger k-point set are done for the six-layer all-free slab, and for the 1x1 cell a 6x6x1 k-point mesh is found to be optimal. In the presence of adsorbate a 2x2 unit cell is used (with a 3x3x1 k-point mesh) to reduce the interaction between periodic images.
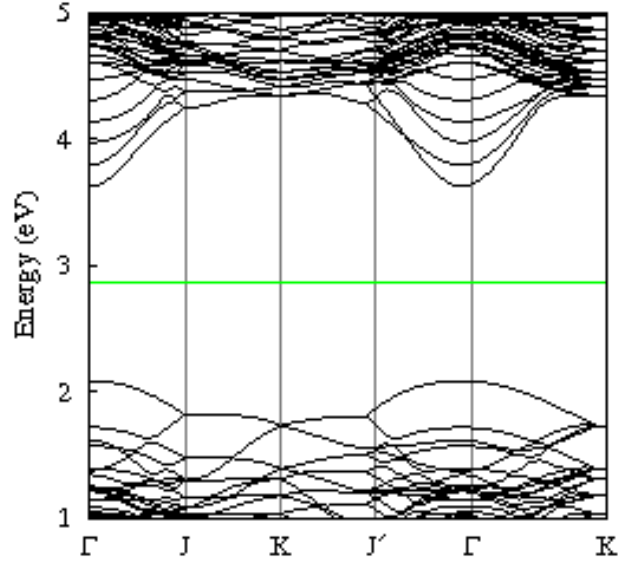

Figure 3.4: Band structure of 2x2 (001) anatase surface along high symmetry directions.

As a further check, a band structure calculation is performed along high-symmetry directions for the 2x2 (001) anatase surface. Obtained band structure is in good agreement with theoretically obtained structure [53].

3.3.2   Anatase (101) Surface

The (101) surface is thermodynamically the most stable anatase surface [55]. It is the most abundant surface configuration, but since stability means low reactivity it is not favorable for catalytic applications. The unit cell of the (101) surface has a triclinic shape, which is obtained by applying Euler rotations to the unit cell of the bulk. The relaxed surface has a saw-tooth like shape with twofold (O1) and threefold (O2, O3) coordinated oxygen atoms, and fivefold (Ti1) and sixfold (Ti2) coordinated titanium atoms, that yield to three oxygen and two titanium atoms per cell on the surface (Figure 3.5). Ratio of the base vectors of the unit cell is 1.45, so 5x3x1, 6x4x1 and 7x5x1 k-point meshes are used for surface energy calculations of
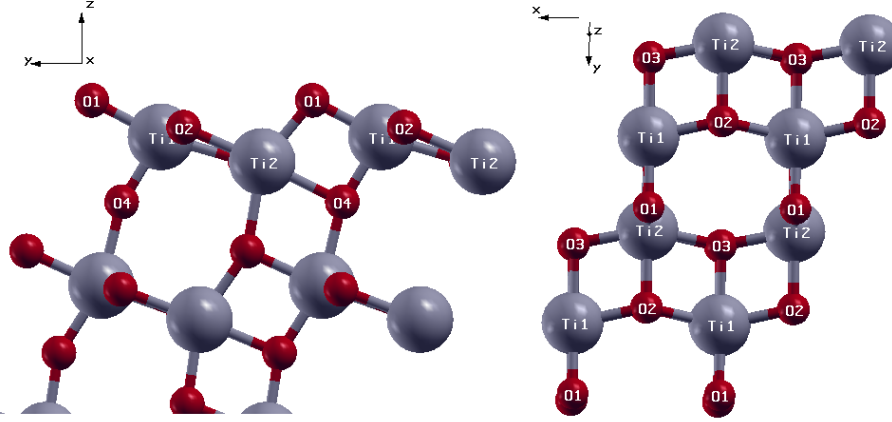
slabs with four, five and six layers.

Figure 3.5: Side and top view of surface atoms of (101) anatase surface.

Very similar surface energies are obtained for the same slabs with different k-points (Table 3.3). It is observed that the difference in the surface energy of partially fixed and "all-free" slabs for the six layered surface is smaller than the four-layer surface, but there are 48 more atoms in the 2x2 cell, which increases the computational cost significantly. Thus for describing the (101) surface as a support, a four-layer slab with two fixed layers is chosen. The calculations are performed with a 3x2x1 k-point mesh.

Table 3.3: Surface energies of (101) anatase surfaces for four, five and six-layer slabs in J/m^2.

Layer/fixed (Eq.)	Ref. [50,51]	5x3x1	6x4x1	7x5x1
4/0 (3.1)	0.45	0.429	0.429	0.429
4/2 (3.2)		0.460	0.460	0.459
4/4 (3.1)		1.159	1.159	1.159
5/0 (3.1)		0.441	0.440	0.440
5/2 (3.2)		0.447	0.446	0.446
5/5 (3.1)		1.160	1.159	1.159
6/0 (3.1)	0.44	0.443	0.442	0.442
6/2 (3.2)		0.442	0.441	0.440
6/3 (3.2)		0.448	0.446	0.446
6/6 (3.1)		1.160	1.159	1.158

Atomic displacements of the relaxed surface contradicts previously reported values but the

bond expansions of surface atoms are in good agreement (Table 3.4).

Table 3.4: Displacements of surface atoms for (101) anatase surface. Apical bonds (a) are 1.995 Å, and equatorial (e) ones are 1.938 Å. Values in parenthesis are from literature [50].

ID	Atomic Displacements (Å)			Bond Expansion	
	[010] (x)	[10$\bar{1}$] (-y)	[101] (z)	Label (type)	%
O1	0.00	0.156 (0.29)	0.051 (-0.02)	Ti1-O1 (a)	-8.2 (-8.6)
O2	0.00	0.070 (0.16)	0.306 (0.19)	Ti1-O2 (e)	+2.2 (+2.0)
O3	0.00	0.040 (0.17)	0.086 (0.06)	Ti1-O3 (a)	+3.2 (+3.3)
O4	0.00	0.075 (0.15)	0.019 (-0.07)	Ti1-O4 (e)	-8.3 (-8.4)
				Ti2-O1 (e)	-4.4 (-5.0)
Ti1	0.00	-0.081 (0.02)	-0.072 (-0.18)	Ti2-O2 (a)	+0.7 (+0.3)
Ti2	0.00	0.055 (0.17)	0.233 (0.20)	Ti2-O3 (e)	-0.1 (-0.3)
Ti3	0.00	-0.084 (-0.04)	-0.025 (-0.14)	Ti3-O4 (e)	+3.8 (+5.2)

3.3.3 (100) Barium Oxide Surface

In NRS systems NO_x molecules are mainly stored on the storage component, which is basically an oxide of alkali and alkali earth metals. Chemical properties of this component play a crucial role in the storage and reduction of NO_x. Interaction with the acidic adsorbate (NO_x) strongly depends on the basicity of the storage component. Since the basicity increases going down in the periodic table (Mg $\rightarrow$ Ba), among alkali and alkali earth metals, the oxide of barium (Ba) is mainly used in commercial NSR experiments.

BaO has a rock salt (NaCl) structure with six-fold coordinated oxygen and barium atoms and its cell-parameters are obtained from the bulk calculations using the same procedure as those used for anatase. The calculated lattice-parameter (5.582 Å) agrees well with previously reported experimental (5.523 Å [56]) and theoretical values (5.608 Å [57]). Free and partially fixed four, five and six layered (100) BaO surfaces were investigated. All surfaces have two five-fold coordinated oxygen atoms and two five-fold coordinated barium atoms per cell. Calculated surface energies (Table 3.5) are in good agreement with previously reported theoretical calculations (0.35 [57], 0.4 [58] J/m^2).

Taking into account these results and the computational costs, five-layer slabs with two fixed layers are used in the rest of the thesis to describe the surface. There are 80 atoms in the
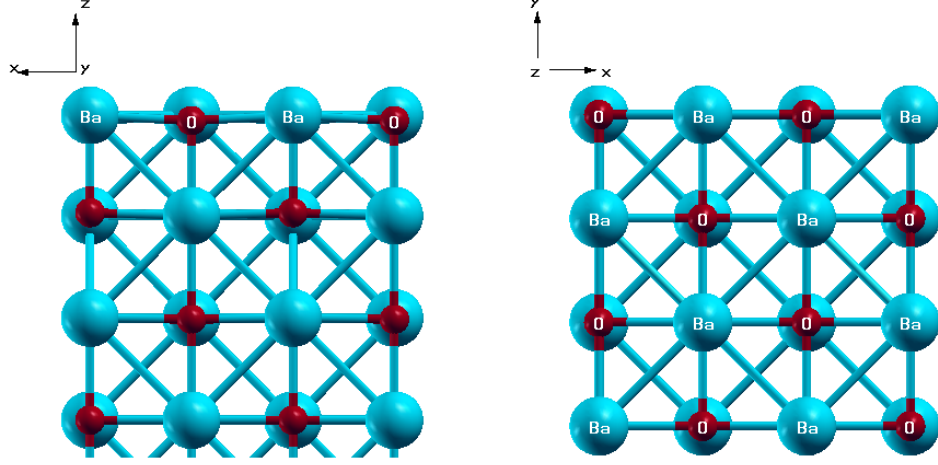
Figure 3.6: Side and top view of surface atoms of (100) BaO surface.

Table 3.5: Surface energies of (100) BaO surfaces for four, five and six-layer slabs in J/m^2.

Eq.	Layer/fixed	E_{surf}	Layer/fixed	E_{surf}	Layer/fixed	E_{surf}
(3.1)	4/0	0.294	5/0	0.317	6/0	0.305
(3.2)	4/2	0.307	5/2	0.311	6/2	0.306
(3.1)	4/4	0.371	5/5	0.371	6/6	0.371

unit cell with fivefold coordinated oxygen and barium atoms on the surfaces (Figure 3.6). The presence of unsaturated bonds is the main reason of surface reactivity. During geometric optimization surface oxygens move inwards causing a mild surface reconstruction referred to as "rumpling". Interlayer distances for the bulk (2.791 Å) and for the top layer of the relaxed surface (2.612 Å for O and 2.675 Å for Ba), surface rumpling (-5.3 %) and relaxation (-2.3 %) of this surface are in a good agreement with reported values [59, 58].

3.4 BaO loadings on Anatase

The amount of active metal oxide on the support material strongly determines the chemical properties of the catalyst. Although anatase is one of the promising candidates to be the support component in NSR catalysts, there is no reported study in literature on its interaction with barium oxide. In this study dimers, mono-layers and bilayers of BaO on an anatase support will be investigated to observe the effect of BaO loading.

3.4.1 BaO unit on (001) Anatase

The smallest possible barium oxide unit that can be studied in a calculation is the BaO unit. Before adsorbing on anatase surfaces properties of the free BaO unit is investigated. Calculations for molecules are performed in a three-dimensional vacuum to prevent interactions between periodic images, similar to vacuums between slabs in surface calculations. Properties of the free BaO dimer is calculated in the 14 Å cubic cell with a kinetic energy cutoff of 40 Ry, and k-point sampling restricted to the Γ-point due to the excessive folding of the Brillouin zone. The calculated bond length (2.003 Å) is in good agreement with experimentally (1.940 Å [60]) and theoretically (2.04 Å [20]) obtained values.

In the adsorption configuration stability of the adsorbate is directly related to the binding energy, which is calculated by subtracting the energy of the free adsorbate and the clean slab from total the energy of adsorbed configuration:

$$E_{bind} = E_{slab+add} - E_{slab} - E_{add} \tag{3.3}$$

Chemical intiution dictates that when the BaO unit is adsorbed on anatase, the barium atom is expected to bind to oxygen sites, and oxygen atoms on titanium sites, thus BaO units are initially put horizontally on the anatase surface. After geometry optimization there are significant changes in configurations of both the anatase surface and the barium oxide unit. Relaxed structure of unit configurations with corresponding band structures are given in Figure 3.7, 3.8 and 3.9. There is no significant change in the band structure of (001) surface, since PDOS analysis for both configurations shows that bands coming from BaO units overlap with the valance bands of the surface.

There are, to the best of our knowledge, no theoretical analysis of BaO adsorption on anatase surfaces. In our study binding energies are found to be 4.80 and 3.96 eV for configurations shown in Figure 3.7 and 3.8 respectively, which are similar to adsorptions on alumina (2.64-4.82 eV [20]). These binding energies are sufficient to resist against a thermal deterioration. Bond length of BaO units on the anatase surface elongated to 2.42 and 2.32 Å on the relaxed configuration and Lödwin charge analysis show that there is a charge transfer of 0.26 and 0.20 |e| from BaO to the anatase surface respectively.
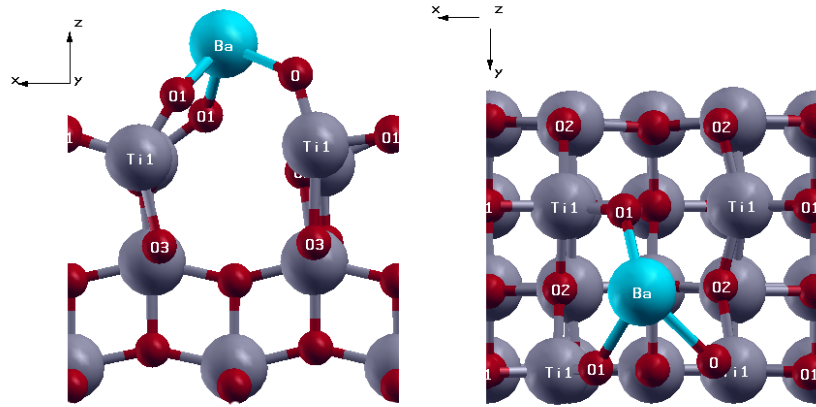
Figure 3.7: Optimized structure of first BaO unit on six-layer (001) anatase surface.
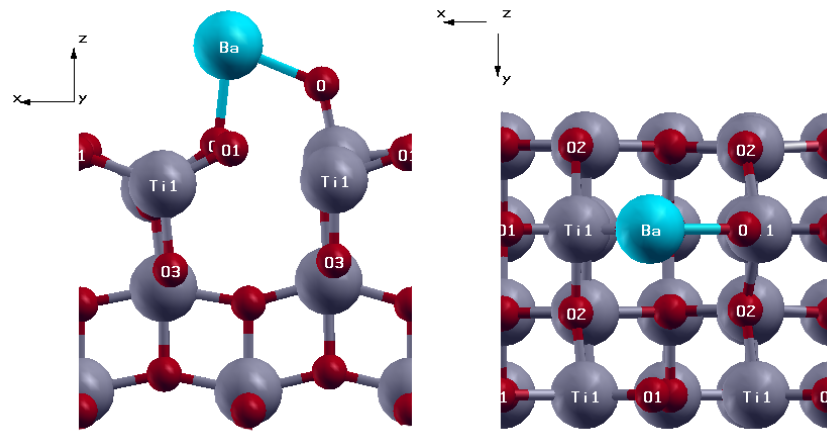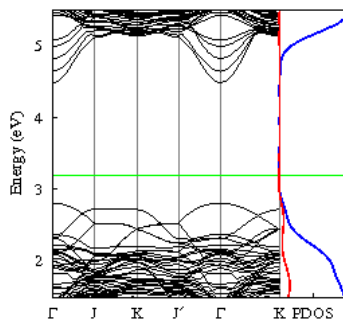

Figure 3.8: Optimized structure of second BaO unit on six-layer (001) anatase surface.
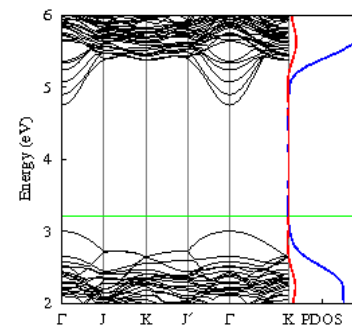
a)   b)

Figure 3.9: Band structure and PDOS analysis of the first and the second BaO unit adsorptions.

3.4.2 BaO layers on (001) Anatase

It is possible to increase the amount of BaO loading to cover all the surface. The cell-parameter of the (100) barium oxide surface was calculated to be 5.58 Å, but it is possible to choose a cell of width of 3.94 Å, which mismatches the cell-parameter of the (001) anatase surface by only 4 %. This gives the opportunity to simulate a few BaO layers epitaxially grown on anatase surface. In such systems two different issues arise that can cause changes in properties of individual components. The first issue is the strain that arises from the mismatch between the lattices of the barium oxide and anatase, and the other issue is electronic property of the system that is due to the different electronic configurations.

Upon addition of the BaO monolayer to the TiO_2 surface and a subsequent geometric relaxation two stable monolayer configurations were obtained (Figure 3.10 a and b). Top views of both configurations are similar to (100) BaO surface, and from the calculated total energies the second configuration is more stable that the first one.

In the first configuration, the BaO monolayer is 2.82 Å above the anatase surface (Figure 3.10 a). Although both the anatase and the barium oxide surfaces are semiconductor individually, band structure calculation shows that the monolayer configuration is metallic. Furthermore, PDOS calculations show that the barium oxide bands that come over the gap of anatase and makes the entire system metallic (Figure 3.11 a).

In the second configuration the BaO layer is 2.03 Å above the anatase surface (Figure 3.10 b). Surprisingly band structure calculations show that the system is a semiconductor, and the PDOS analysis indicates that the bands that arise from BaO layer comes over the valance bands of anatase which do not make any significant change (Figure 3.11 b). This interesting result is probably not due to strain because in both configurations the mismatch between the BaO lattice and anatase lattice is small.
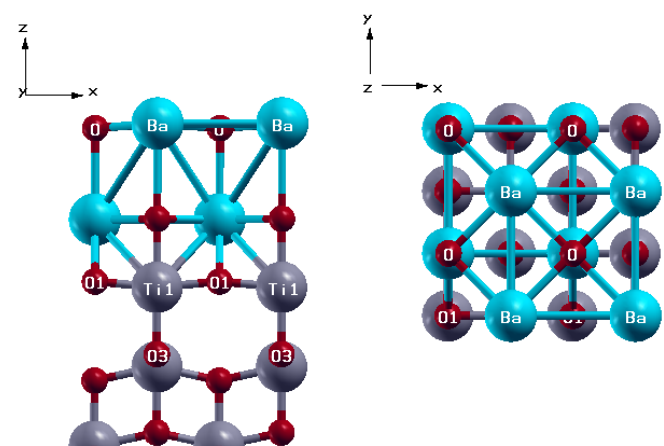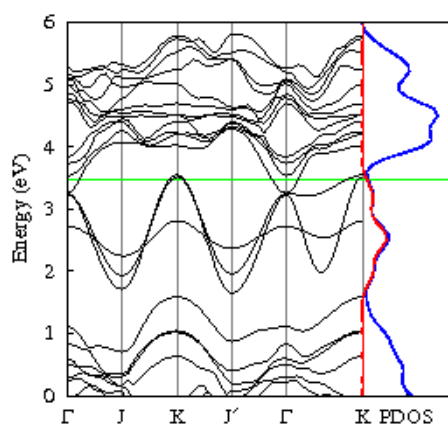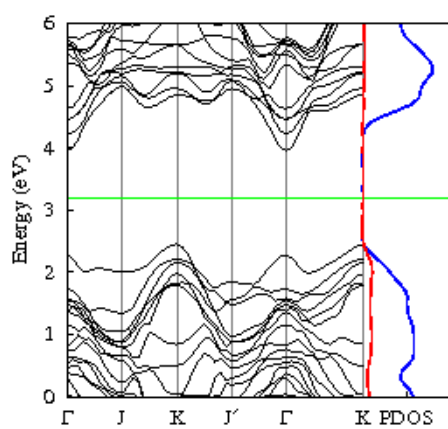
a)
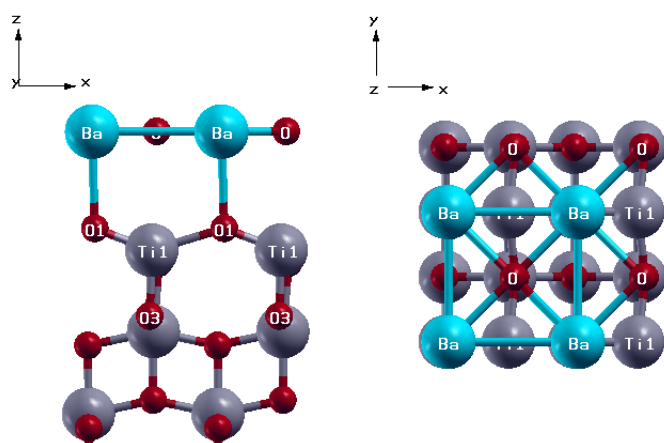
b)
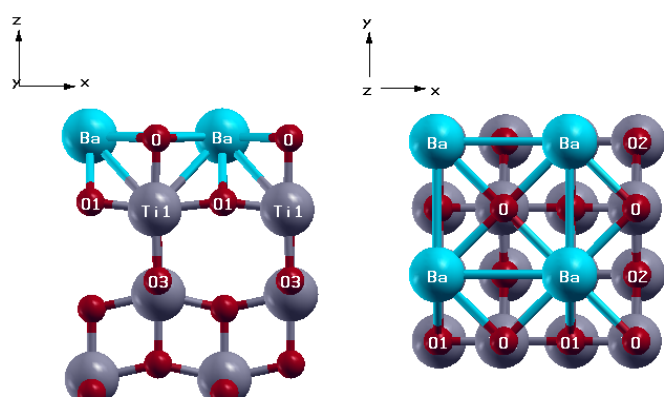
c)

Figure 3.10: Side and top views of optimized monolayer and bilayer BaO configurations on the (001) anatase surface.
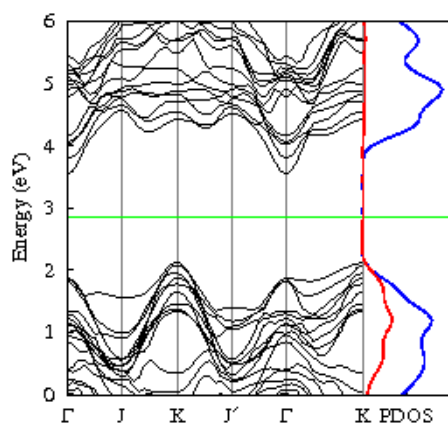
33

a)

b)

c)

Figure 3.11: Band structure and PDOS analysis of optimized monolayer and bilayer BaO configurations on the (001) anatase surface.

To gain further insight into larger BaO loadings or large BaO cluster formations a second layer is placed on both of the above monolayer configurations. For the first configuration barium oxide layers move away from the surface and it s not possible to get a stable bilayer configuration. This is expected due to the already weak bonding in the monolayer case. For the second configuration a stable bilayer barium oxide loading is obtained (Figure 3.10 c). The first layer is 2.08 Å above the anatase, which is slightly larger than the second monolayer configuration, and the surface Ba atom is 2.90 Å away from the oxygen atom below which was 2.68 Å in the five layer (100) BaO surface. Moreover, band structure and PDOS calculations indicate that bands coming from the BaO layers overlap the conduction bands of TiO_2 similarly to the second monolayer configuration (Figure 3.11 c).

3.5 NO$_2$ and SO$_2$ Adsorptions

There are two possible NO_x species in the exhaust: NO and NO_2. Since NO mostly oxidizes to NO_2 in the presence of oxygen during the lean period, here only adsorption of NO_2 will be considered. Properties of free NO_2 and SO_2 are calculated in the 14 Å vacuum cubic cell, with kinetic energy cutoff of 40 Ry and at the Γ-point. Calculated molecular structure for NO_2 (1.212Å, 134°) and SO_2 (1.459Å, 119°) is in a good agreement with previously obtained experimental (1.193Å, 134.1° and 1.1432 Å, 119.5° [61]), and theoretical values (1.213Å, 133.7° and 1.454Å, 119.5°) for NO_2 [59] and SO_2 [57].

Stability of the adsorbate on the storage component is very crucial, because weakly adsorbed NO_2 can desorb before being reduced to the harmless compounds. Thus adsorption of NO_2 on different BaO configurations have already been investigated by using DFT [62,63]. There are different binding energies reported for the same adsorption configurations, but relative stabilities are similar, that probably arise from different calculation methods and technical details. Schneider et al. [57] investigated the adsorption of NO_2 on alkaline earth metal oxide surfaces and compared them with the adsorptions of SO_2 and CO_2. They report that SO_2 is acidic and chemisorbs on basic O_s site on the surface (Figure 3.12 d), whereas it is possible for NO_2 to adsorb as acidic, basic and ionic, and adsorptions of NO_2 are weaker than SO_2. There are two "N-down" configurations with short (Figure 3.12 a) and long (Figure 3.12 b) N-O_s bonds and one bridge (Figure 3.12 c) configuration with two O-Ti$_s$ bonds.
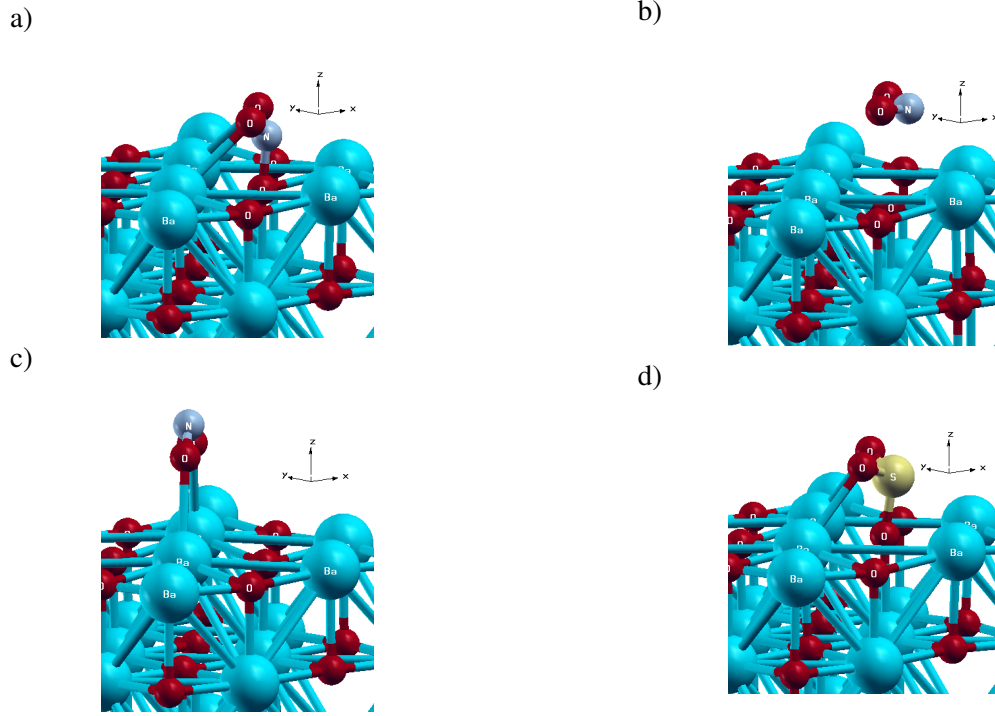
Figure 3.12: NO$_2$ and SO$_2$ adsorptions on (100) BaO surface.

Table 3.6: Adsorption properties of NO$_2$ and SO$_2$ on unsupported (100) BaO surfaces. Schneider's [57] results in parenthesis.

Adsorption	E$_{bind}$ [eV]	d$_{ad-S}$ [Å]	α [°]	r$_{A-O}$ [Å]	$\Delta\rho$ [|e|]
Fig. 3.12 a	1.62 (1.52)	1.45 (1.44)	121 (121)	1.32 (1.32)	0.90
Fig. 3.12 b	1.49 (1.47)	2.72 (2.66)	117 (117)	1.27 (1.28)	0.85
Fig. 3.12 c	1.43 (1.43)	2.77 (2.75)	117 (116)	1.27 (1.28)	0.80
Fig. 3.12 d	2.66 (2.60)	1.64 (1.64)	111 (104)	1.52 (1.52)	0.53

Calculated stabilities and adsorption configurations of NO$_2$ and SO$_2$ in our study are in good agreement with Schneider's work (Table 3.6). Thus the binding energy of SO$_2$ is significantly larger than any NO$_2$ adsorption configuration; that is explained by the relatively strong acidity of SO$_2$ molecule. On the other hand, the charge transfer from the surface to the NO$_2$ molecule in this calculation shows that all adsorptions are acidic. Moreover, for all configurations N–O bonds elongated; this is due to decrease in an inter-atomic force which is related with charge difference of nitrogen and oxygen atoms. Moreover, the ONO angle decreased, which means the amount of charge difference on the oxygen atoms decreased.

For the adsorptions on the first monolayer configuration (Figure 3.13) adsorption properties are effected differently. Calculated binding energies indicate that stability of the first and second configuration increases, while it was found to decrease for the third configuration and for the SO_2 adsorption. At the same time, the first configuration moves closer to the surface, while second and third ones move away. Geometric properties of adsorbents do not change appreciably, but the displacement of the surface oxygen on the surface increase (Table 3.7).

a)

b)

c)

d)

Figure 3.13: NO_2 and SO_2 adsorptions on first anatase-supported BaO monolayer configuration.

Table 3.7: Adsorption properties of NO_2 and SO_2 on first anatase-supported BaO monolayer configuration.

Adsorption	E_{bind} [eV]	d_{ad-S} [Å]	α [°]	r_{A-O} [Å]	$\Delta\rho$ [|e|]
Fig. 3.13 a	1.98	1.34	126	1.25	0.71
Fig. 3.13 b	1.64	2.84	117	1.27	0.31
Fig. 3.13 c	1.28	2.79	118	1.26	0.72
Fig. 3.13 d	2.44	1.67	110	1.52	0.52

On the second type of monolayer configuration stability of all adsorbents (Figure 3.14) are effected negatively despite significant charge transfers from the surface. Moreover, stabilities of NO_2 adsorbents decrease more than stability of SO_2 adsoption. Geometrical structure of adsorbents are very close to the geometric structures on the bulk BaO, and there is similar displacements for the surface oxygen atom, but the distances to the surface atom change for the second and third NO_2 adsorptions (Table 3.8).
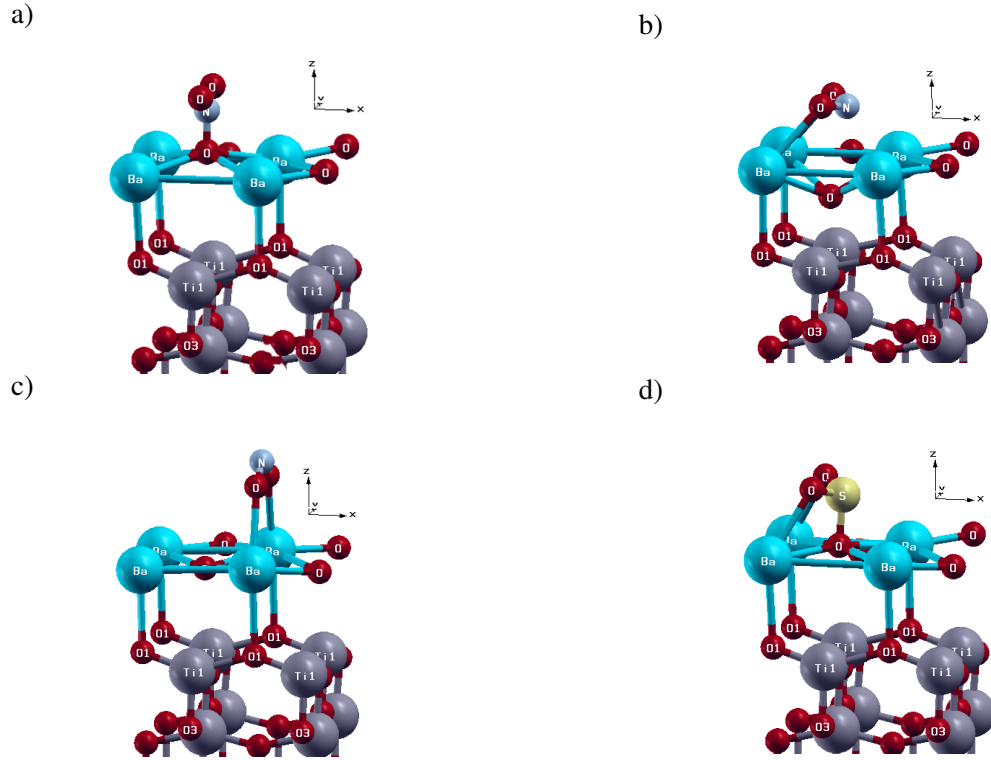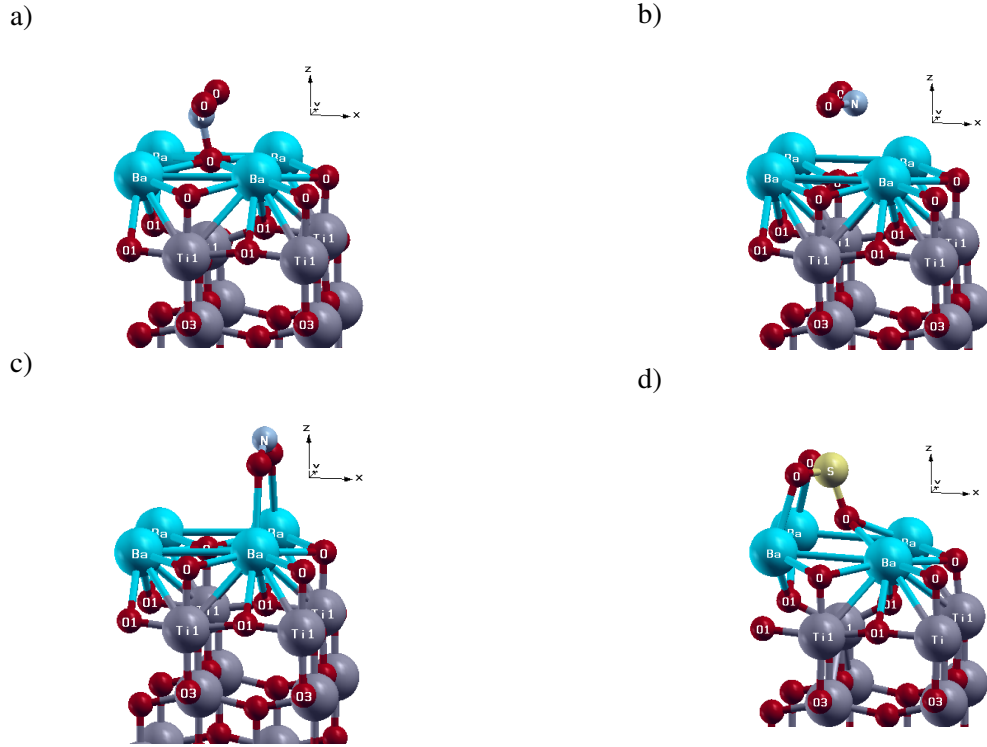
a)

b)

c)

d)

Figure 3.14: NO_2 and SO_2 adsorptions on second anatase-supported BaO monolayer configuration.

Table 3.8: Adsorption properties of NO_2 and SO_2 on second anatase-supported BaO monolayer configuration.

Adsorption	E_{bind} [eV]	d_{ad-S} [Å]	α [°]	r_{A-O} [Å]	$\Delta\rho$ [$|e|$]
Fig. 3.14 a	1.09	1.45	123	1.31	0.82
Fig. 3.14 b	1.25	2.63	117	1.27	0.78
Fig. 3.14 c	1.12	2.83	119	1.26	0.75
Fig. 3.14 d	2.62	1.66	108	1.53	0.54

Calculated binding energies for the adsorptions on the bilayer BaO supported by anatase (Figure 3.15) indicate that stabilities were decreased for all NO_2 adsorptions similar to adsorptions

on the second monolayer configurations, but there is significant decrease in SO_2 stability (Table 3.9). Moreover, adsorption geometries for all adsorptions on bilayer configuration are very close to adsorption geometries on the unsupported BaO.
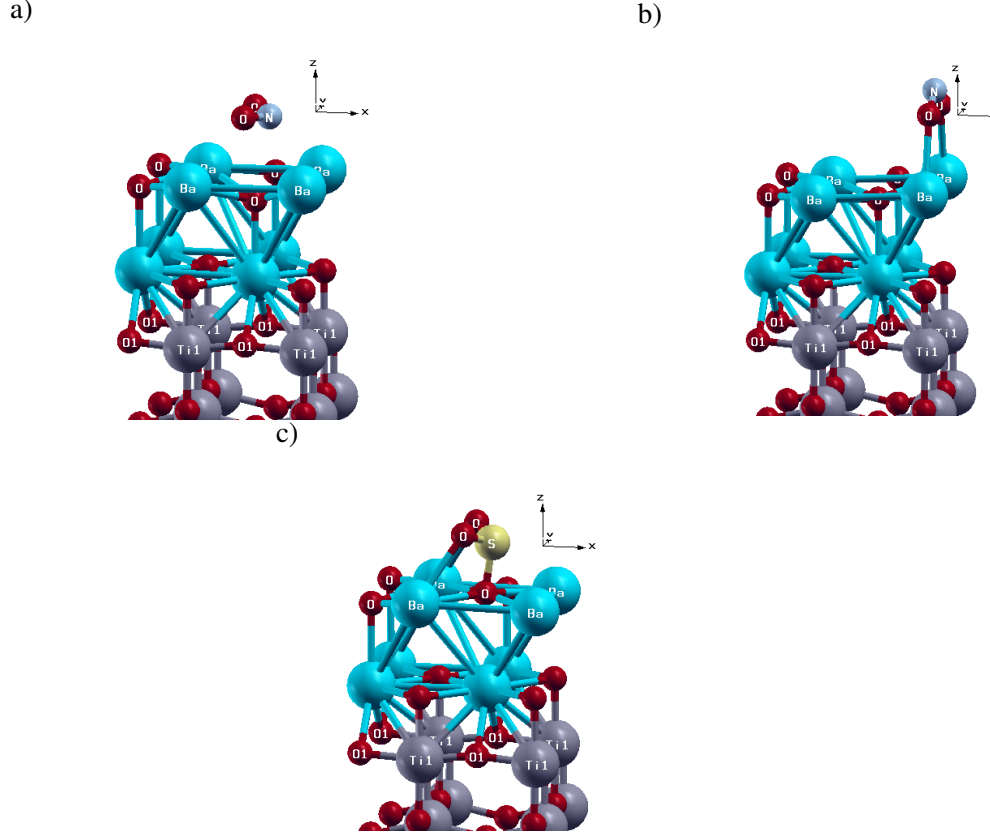
a)

b)

c)

Figure 3.15: NO_2 and SO_2 adsorptions on anatase-supported BaO bilayer configuration.

Table 3.9: Adsorption properties of NO_2 and SO_2 on anatase-supported BaO bilayer configuration.

Adsorption	E_{bind} [eV]	d_{ad-S} [Å]	α [°]	r_{A-O} [Å]	$\Delta\rho$ [|e|]
Fig. 3.15 a	1.37	2.78	117	1.27	0.85
Fig. 3.15 b	1.11	2.72	117	1.27	0.72
Fig. 3.15 c	2.09	1.68	112	1.52	0.48

From these results it can be concluded that stabilities of adsorbate on the anatase supported BaO layers are strongly dependent on electronic properties. First anatase supported BaO monolayer catalyst showed advantage by increase in stabilities of NO_2 adsorptions with the same time decrease in stability of SO_2 adsorption. That catalyst differed from the other two catalysts with its metallic band structure.

CHAPTER 4

CONCLUSION

Transportation is the one of the indispensable requirements of daily life. Environmental and health issues resulting from the exhaust of vehicles force the development of technology for emission control. NO_x storage-reduction catalysts were developed to convert harmful nitrogen oxides in the exhaust of gasoline and diesel engines working in lean condition to harmless oxygen and nitrogen gases. Several theoretical and experimental investigations on different catalyst components have been carried out to develop this technology. In this thesis anatase polymorph of titanium dioxide was investigated as a support component of NSR.

Before loading any storage component suitable surfaces must be obtained. Lattice-parameters were obtained from the bulk calculations and (001) and (101) surfaces with different number of layers were constructed with those lattice parameters and with atomic positions that were taken from the bulk by truncation. Displacements as a result of surface reconstructions after relaxations were in good agreement with previously reported values. Moreover, appropriate slab and k-point sampling for further calculations were decided upon by comparing the surface energies.

Interaction of storage component with the support material plays a crucial role in the performance of the catalysts. Therefore, interaction of BaO units on six-layer anatase surface were studied. Binding energies of units on the surface were high enough for the stability at high temperatures. Moreover, epitaxial BaO mono-layers were constructed over four-layer anatase slabs. Two different mono-layer configurations were obtained with completely different electronic properties, thus in one of them bands coming from BaO layer make the system

metallic. Furthermore, the growth of one more BaO layer was attempted to be grown over these mono-layers, but this was possible only on the semiconductor configuration.

Finally the effect of anatase on stabilities of NO_2 and SO_2 on the (100) BaO surface were examined. Firstly, NO_2 and SO_2 were adsorbed on unsupported (100) BaO surface. Binding energies and adsorption geometries were in good agreement with previously reported values for the same configurations. Then NO_2 and SO_2 were adsorbed on anatase supported monolayer and bilayer BaO surfaces with the same configurations and binding energies and geometries were compared. It is observed that adsorption configurations remain similar to the adsorptions on the unsupported (100) BaO surface, which is directly related to similar charge transfers from the catalysts to the adsorbate. On the other hand, changes in the stabilities vary for different systems. It was observed that TiO_2 does not negatively effect stabilities of NO_2 on the (100) BaO surface significantly for all the systems. Moreover, only for the first anatase supported BaO monolayer catalyst, binding energies of NO_2 adsorptions increased, whereas binding energy of SO_2 decreased. That catalyst differed from the others with its metallic band structure.

REFERENCES

[1] G. Centi, P. Ciambelli, S. Perathoner, P. Russo, Catal. Today **75**, 3 (2002).

[2] C. K. N. Patel, E. G. Burkhardt, C. A. Lambert, Science **184**, 1173 (1974).

[3] R. Impens, Stud. Surf. Sci. Catal. **30**, 11 (1987).

[4] A. Fritz, V. Pitchon, Appl. Catal. B **13**, 1 (1997).

[5] M. Chiron, Stud. surf. Sci. Catal **30**, 1 (1987).

[6] V. Vestreng, K. Mareckova, S. Kakareka, A. Malchykhina, T. Kukharchyk, EMEP technical report, 1 (2007).

[7] V. Vestreng, L. Ntziachristos, A. Semb, S. Reis, I. S. A. Isaksen, L. Tarrason, Atmos. Chem. Phys. **9**, 1503 (2009).

[8] R. T. Yang, W. B. Li, N. Chen, Appl. Catal. A **169**, 215 (1998).

[9] J. C. Schatler, P. J. Mitchell, Ind. Eng. Chem. Prod. Res. Dev. **19**, 288 (1980)

[10] S. Matsumoto, Cattech **4/2**, 102 (2000).

[11] J. H. Kwak, D. H. Kim, T. Szailer, C. H. F. Peden, J. Szanyi, Catal. Lett. **111**, 119 (2006).

[12] I. Nova, L. Castoldi, L. Lietti, E. Tronconi, P. Forzatti, Catal. Today **75**, 431 (2002).

[13] D. H. Kim, Y. H. Chin, G. G. Muntean, A. Yezeretz, N. W. Currier, W. S. Epling, H. Y. Chen, H. Hess, C. H. F. Peden, Ind. Eng. Chem. Res. **45**, 8815 (2006).

[14] Y. Su, K. S. Kabin, M. P. Harold, M. D. Amiridis, App. Catal. B **71**, 207 (2007).

[15] J. G. Kim, H. M. Lee, M. J. Lee, J. H. Lee, J. G. Kim, J. Y. Jeon, S. K. Jeong, S. J. Yoo, S. S. Kim, J. Ind. Eng. Chem. **14**, 841 (2008).

[16] J. Jelic, R. J. Meyer, Catal. Today **136**, 76 (2008).

[17] Y. Sakamoto, S. Matsunaga, K. Okumura, T. Kayama, K. Yamazaki, N. Takahashi, T. Tanaka, Y. Kizaki, T. Motohiro, H. Shinjoh, Chem. Eng. Sci. **63**, 5028 (2008).

[18] L. Cheng, Q. Ge, J. Phys. Chem. C **112**, 16924 (2008).

[19] M. Piacentini, M. Maciejewski, A. Baiker, Appl. Catal. B **72**, 105 (2007).

[20] D. Mei, Q. Ge, J. H. Kwak, D. H. Kim, J. Szanyi, C. H. F. Peden, J. Phys. Chem. C **112**, 18050 (2008).

[21] J. H. Kwak, D. Mei, C. W. Yi, D. H. Kim, C. H. F. Peden, L. F. Allard, J. Szanyi, J. Catal. **261**, 17 (2009).

[22] P. Broqvist, H. Gröbeck, Surf. Sci. **600**, L214 (2006).

[23] M. Andonova, G. S. Sentük, E. Kayhan, E. Özensoy, J. Phys. Chem. C **113**, 11014 (2009).

[24] J. Despres, M. Koebel, O. Kröher, M. Elsener, A. Wolaun, Appl. Catal. B **43**, 389 (2003).

[25] L. Li, Q. Shen, J. Cheng, Z. Hao, Catal. Today (in press), (2010).

[26] S. Takahashi, A. Suda, I. Hachisuka, M. Sugiura, H. Sobukawa, H. Shinjoh, Appl. Catal. B **72**, 187 (2007).

[27] M. Born, R. Oppenheimer, Ann. Phys. **84**, 457 (1927).

[28] P. Philips, Advanced Solid State Physics, Westview Press, (2003).

[29] L. H. Thomas, Proc. Cambridge Phil. Soc. **23**, 542 (1927).

[30] E. Fermi, Rend. Accad. Naz. Linzei **6**, 602 (1927).

[31] K. Burke, ABC of DFT, Avaible at http://chem.ps.uci.edu/~kieron/dft/book/, (2007).

[32] P. Hohenberg, W. Kohn, Phys. Rev. **136**, B864 (1964).

[33] W. Kohn, L. J. Sham, Phys. Rev.**140**, A1133 (1965).

[34] D. M. Ceperley and B. J. Alder, Phys. Rev. Lett. **45**, 566 (1980).

[35] D. R. Hamann, M. Schlüter, C. Chiang, Phys. Rev. Lett. **430**, 1494 (1979).

[36] D. Vanderbilt, Phys. Rev. B **41**, 7892 (1990).

[37] Avaible at http://www.quantum-espresso.org/, with General Public Licence (2010).

[38] H. Hellmann, Einführung in die Quantenchemie 285 (1937).

[39] R. P. Feynman, Phys. Rev. **56**, 340 (1959).

[40] D. W. Snoke, Solid State Physics: Essential Concepts, Addison Wesley, (2008).

[41] Avaible at http://www.xcrysden.org/, with General Public Licence (2010).

[42] M. Springborg, Methods of electronic-structure calculations: from molecules to solids, Jhon Wiley, (2000).

[43] J. P. Perdew, K. Burke, and M. Ernzerhof, Phys. Rev. Lett. **77**, 3867 (1996).

[44] W. D. Brown, W. W. Grannenmann, Solid State Elecron. **21**, 837 (1978).

[45] K. L. Siefering, G. L. Griffin, J. Electrochem. Soc. **73**, 1206 (1990).

[46] G. Wakefield, J. Stott, J. Cosmet. Sci. **57**, 385 (2006).

[47] K. Rajeswar, J. Appl. Electrochem. **15**, 1 (1985).

[48] K. I. Hadjiivanov, D. G. Klissurski, Chem, Soc. Rev. **25**, 61 (1996).

[49] J.K. Burdett, T. Hughbanks, G. J. Miller, J. W. Richardson, Jr., J. V. Smith, J. Am. Chem. Soc. **109**, 3639 (1987).

[50] M. Lazzeri, A. Vitttadini, A. Selloni, Phys.Rev B **63**, 155409 (2001).

[51] M. Lazzeri, A. Vitttadini, A. Selloni, Phys.Rev B **65**, 119901(E) (2002).

[52] H. Tang, H. Berger, P. E. Schmid, F. Levy, G. Burri, Solid State Commun. **87**, 847 (1999)

[53] E. Mete, D. Uner, O. Gürseren, Ş. Ellialtioğlu, Phys. Rev. B **79**, 125418 (2009).

[54] M. Calatayud, C. Minot, Surf. Sci. **552**, 169 (2004).

[55] U. Diebold, Surf. Sci. Rep. **48**, 53 (2003).

[56] R. W. G. Wyckoff, Crystal Structures, Wiley, (1963).

[57] W. F. Schneider, J. Phys. Chem. B **108**, 273 (2004).

[58] P. Broqvist, I. Panas, H. Grönbeck, J. Phys. Chem. B **109**, 15410 (2005).

[59] M. Tutuianu, O. R. Indervildi, W. G. Bessler, J. Warnatz, J. Phys. Chem. B **110**, 17484 (2006).

[60] G. Herzberg, Molecular Spectra and Molecular Structure I. Spectra of Diatomic Molecules, D. Van Nostrand Comp., Princeton, (1950).

[61] G. Herzberg, Molecular Spectra and Molecular Structure III. Electronic Spectra and Electronic Structure of Polyatomic Molecules, D. Van Nostrand Comp., Princeton, (1967).

[62] M. M. Branda, C. D. Valentin, G. Pacchoni, J. Phys. Chem. B **108**, 4752 (2004).

[63] H. Grönbeck, P. Broqvist, I. Panas, Surf. Sci. **600**, 403 (2006).